nature communications

Article

https://doi.org/10.1038/s41467-026-69849-4

Transforming disorder in the design of advanced high-entropy oxide electrocatalysts for zinc-air batteries

Received: 7 August 2024

Accepted: 11 February 2026

Published online: 23 February 2026

Check for updates

Xiaoran Zheng[1] ✉, Sajjad S. Mofarah[1] ✉, Richard F. Webster[1,2], Jinqiang Zhang[3], Claudio Cazorla[4,5], Yan Nie[6], Shuhao Wang[6], Yue Jiang[1], Thibault De Villenoisy[1], Jinbo Wang[1], Yin Yao[2], Tingwen Zhao[6], Liming Dai[7], Shery L. Y. Chang[1,2], Chuan Zhao[6], Dewei Chu[1], Leigh Sheppard[8], Pramod Koshy[1] ✉ & Charles C. Sorrell[1]

Research on high-entropy oxides generally is limited to elemental and structural interpretations applied to the performance of cathodes. However, there are only limited data on the principles of increasing disorder in terms of structural, electronic, and atomic mechanisms as materials convert from ordered to disordered. Zn-air battery cathodes are limited by slow kinetics, imbalanced oxygen evolution reaction charging, imbalanced oxygen reduction reaction discharging, and scalability (through the necessity of benchmark noble metals). The present work pioneers the engineering of multilevel disorder in high-entropy oxides, thereby transforming an intrinsically inactive matrix into a highly active cathode. Systematic modification of the disorder through increasing number of cations leads to the abrupt development of structural (2D defects), electronic (semimetallic conductivity), and atomic (low-coordination Ce) disorder. This multilevel disorder engineering of high-entropy oxides results in MnNiCoFe-CeO_2 catalysts with stable active sites, rapid and balanced bifunctional (oxygen evolution/reduction reaction) performance, thereby promising Zn-air battery efficiencies and electrochemical durabilities greater than those of the benchmark materials).

High-entropy oxides (HEOs) are an emerging class of chemically-complex, single-phase, solid solutions containing at least five different cations[1,2]. They have high configurational entropies arising from their disordered multicomponent oxide systems. These establish an infinite number of tuneable permutations of elemental combinations through structural, electronic, and atomic hybridizations, allowing multifunctional materials design for catalytic and other energy-storage applications[3–5].

The distinctive features of HEOs enable the development of bifunctional catalysts that are well suited for alkaline conditions owing to their corrosion resistance from hydroxides, where metals and non-oxides are subject to such corrosion[6]. These attributes establish HEOs

[1]School of Materials Science and Engineering, UNSW Sydney, Sydney, NSW, Australia. [2]Electron Microscopy Unit (EMU), Mark Wainwright Analytical Centre, UNSW Sydney, Sydney, NSW, Australia. [3]Centre for Clean Energy Technology, School of Mathematical and Physical Sciences, University of Technology Sydney, Sydney, NSW, Australia. [4]Departament de Física, Universitat Politècnica de Catalunya, Barcelona, Spain. [5]Institució Catalana de Recerca i Estudis Avançats (ICREA), Barcelona, Spain. [6]School of Chemistry, UNSW Sydney, Sydney, NSW, Australia. [7]School of Chemical Engineering, UNSW Sydney, Sydney, NSW, Australia. [8]Solar Energy Technologies Research Group, Western Sydney University, Penrith, NSW, Australia. ✉e-mail: xiaoran.zheng@unsw.edu.au; s.seifimofarah@unsw.edu.au; koshy@unsw.edu.au

as promising candidates for cathodes in zinc-air batteries (ZABs), where the oxygen evolution reaction (OER) governs charging, and the oxygen reduction reaction (ORR) drives discharging. The benchmark cathodes still are dominated by noble-metal catalysts ($Pt/C+IrO_2$) owing to its corrosion resistance and well-suited catalytic activity with balanced OER/ORR kinetics[7]. Most design strategies for high-performance cathodes are based on composites, combining OER-favorable (e.g., NiFe-based) with ORR-favorable (e.g., noble metal/carbon-based) materials[8–10]. While this composite approach seeks to capitalize on the strengths of each component, it frequently suffers from significant kinetic or performance imbalances between OER and ORR[7]. This limitation is likely due to the focus on optimization of one aspect of catalytic performance while overlooking the critical need for balanced kinetics and activity between the two reactions. Therefore, this necessitates the development of advanced electrocatalysts capable of bifunctionality, effectively accelerating both OER and ORR by optimizing their reaction mechanisms.

OER mechanisms are well-documented, involving actives sites in the form of redox-capable cations and lattice oxygen[11]. The ORR mechanism remains uncertain, particularly for oxide-based catalysts[12]. It has been shown recently that the ORR mechanism for pure metal catalysts may involve oxygen gas adsorption on metal surfaces and that this is facilitated by the existence of unpaired electrons of the metal ions, where each oxygen molecule requires two unpaired electrons from the metal site for bond formation[13]. CeO_2 is a promising material well-suited for OER owing to $Ce4f^0$ to $Ce4f^1$ redox electron transfer, intrinsic point defect formation (Ce^{3+}), and charge-compensating oxygen vacancies[14]. However, CeO_2 is a wide-band-gap semiconductor, resulting in poor charge transfer between CeO_2 and active sites for OER/ORR in ZABs. Transition metal (TM) doping can alter the *d* band center to improving the charge transfer, which can activate reactive species adsorption[15]. Further, CeO_2 exhibits a large solid solubility range, making it an potential candidate for the development of HEOs[16].

There are four recognized key effects in HEOs: high-entropy effect, lattice distortion effect, sluggish-diffusion effect, and cocktail effect[17]. Of these, lattice distortion has attracted the most attention owing to its strong influence on the overall material properties. This effect originates from the coexistence of multiple cations of varying ionic radii, valence states, electronegativities, and coordination within the same sublattice. These coexistences cause atomic mismatches, which can lower the symmetry of the unit cell; introduce lattice distortion and strain; and generate 0D, 1D, 2D, and 3D defects, which may require charge compensation[18]. Further, the distances between neighboring ions occur over a distribution rather than at fixed values, thus placing the structure in a thermodynamically nonequilibrium state[17]. This deviation can lower the energy barriers for molecular adsorption, activation, and OER/ORR conversion in electrocatalytic reactions[19]. Despite the significance of lattice distortion, the current understanding of such disorder in HEOs remains limited[20,21]. Most studies focus primarily on identifying high concentrations of defects (e.g., oxygen or metal vacancies) and the absence of long-range order[21,22]. However, a comprehensive analysis of disorder from a structural, electronic, and atomic perspective remains lacking. In particular, there is a need for a systematic correlation of this multilevel disorder with the corresponding electrocatalytic performance, especially for bifunctional OER/ORR catalysts for ZABs. The present work explores this correlation through the performance of ZABs, with the aim of elucidating the mechanisms of the roles of disorder in HEO in governing catalytic activity.

To the preceding aim, the present work introduces a different non-noble-metal MnNiCoFe-CeO_2 -based HEO and a conceptual mechanistic framework that facilitates simultaneous improvement in multilevel disorder through structural-, electronic-, and atomic-level disorders, leading to improvement in the OER/ORR activities as well as promising performance and stability in ZABs. This analysis provides a platform for the application of disorder engineering in the design of systematic ranges of progressively more complex systems, from individual oxides to HEOs.

Results and discussion

Structural disorder

The fabrication strategy involves a simple approach to HEO self-assembly at room temperature (Fig. 1a). A Ce-based coordination polymer $Ce(TCA)_2(OH)_2{\cdot}2H_2O$ (Ce-CP) and different *3d*-TM salts were dissolved in a polar aqueous ethanol solution to yield nanospheres of the nominal composition $Mn_{0.035}Ni_{0.035}Co_{0.035}Fe_{0.035}Ce_{0.860}O_2$, as confirmed by Supplementary Table 1. The Cl^- ions on the Ce-CP surface facilitate electrostatic interactions with TM^{X+} ions[23]. The resultant atomic-scale mixing and strong attraction enable metastable solid solubilities that are retained during room-temperature oxidation and dechlorination in aqueous alkaline solution, leading to the formation of complex HEOs.

With stepwise building and structural development of HEOs can be examined by X-ray diffraction (XRD) (Fig. 1b). Mn addition to CeO_2 (Mn-CeO_2) results in the formation of Mn_3O_4 precipitates, which suggests the exceeding of the solubility limit of Mn in CeO_2. However, subsequent addition of Ni^{2+}, Co^{2+} (MnNiCo-CeO_2), and Fe^{3+} (MnNiCoFe-CeO_2) caused a reversion to homogeneous, single-phase, cubic, solid solutions. This implies that the homogeneity regions of the more complex solid solutions are larger than that for single-element-doped (Mn) alone. Rietveld-peak refinement data (Fig.1c, Supplementary Tables 2-3, and Supplementary Fig. 1) reveal in-depth structural information. In structural analysis, peak shifts in diffraction patterns reflect changes in lattice dimensions while peak broadening is indicative of alterations in crystallinity, often linked to crystallite size. However, other factors, such as dislocation density and strain, which can be used to represent the extent of lattice distortion and so reflect structural disorder, generally are overlooked. These factors provide significant clues in the understanding of defect density and consequent structural disorder. Comprehensive analysis of all of this lattice information suggests that, as the number of TMs increases, the crystallite size decreases while lattice distortion (quantified through dislocation density and microstrain) increases. In order to decouple the effects of crystallite size and lattice distortion, high-resolution transmission electron microscopy (HRTEM) images (Supplementary Fig. 2) are used to illustrate that there is little variation between the observed crystallite sizes of CeO_2 and high-entropy MnNiCoFe-CeO_2 and that the crystallite size remains essentially constant from the bulk to the surface. These data thus confirm that the lattice distortion associated with the structural disorder in MnNiCoFe-CeO_2 derives from increased dislocation density and microstrain rather than a decrease in crystallite size. Therefore, it is possible to isolate the lattice distortion and structural disorder in HEOs, as shown in Fig. 1c. The introduction of the single cation Mn results in the formation of a secondary phase, with minimal structural alteration to the primary matrix. This indicates limited interaction between the host lattice and the added Mn ions, thus maintaining the overall lattice stability. In contrast, the formation of a solid solution, with the addition of three cations (Mn, Ni, and Co), is accompanied by moderate changes in lattice parameters. This alteration likely represents the onset of matrix structural disorder, as the varying ionic radii and bonding characteristics of the cations introduce localized strain and lattice distortion. These changes suggest the beginning of a more complex multielement interaction, setting the stage for enhanced structural heterogeneity and the characteristic lattice distortion observed in HEOs. After the addition of the fifth element (Fe), there was an exponential change in the lattice parameter, indicative of a high degree of lattice distortion and structural disorder.

Further, these highly distorted and disordered structures can be observed clearly in the selected area electron diffraction (SAED)

https://doi.org/10.1038/s41467-026-69849-4

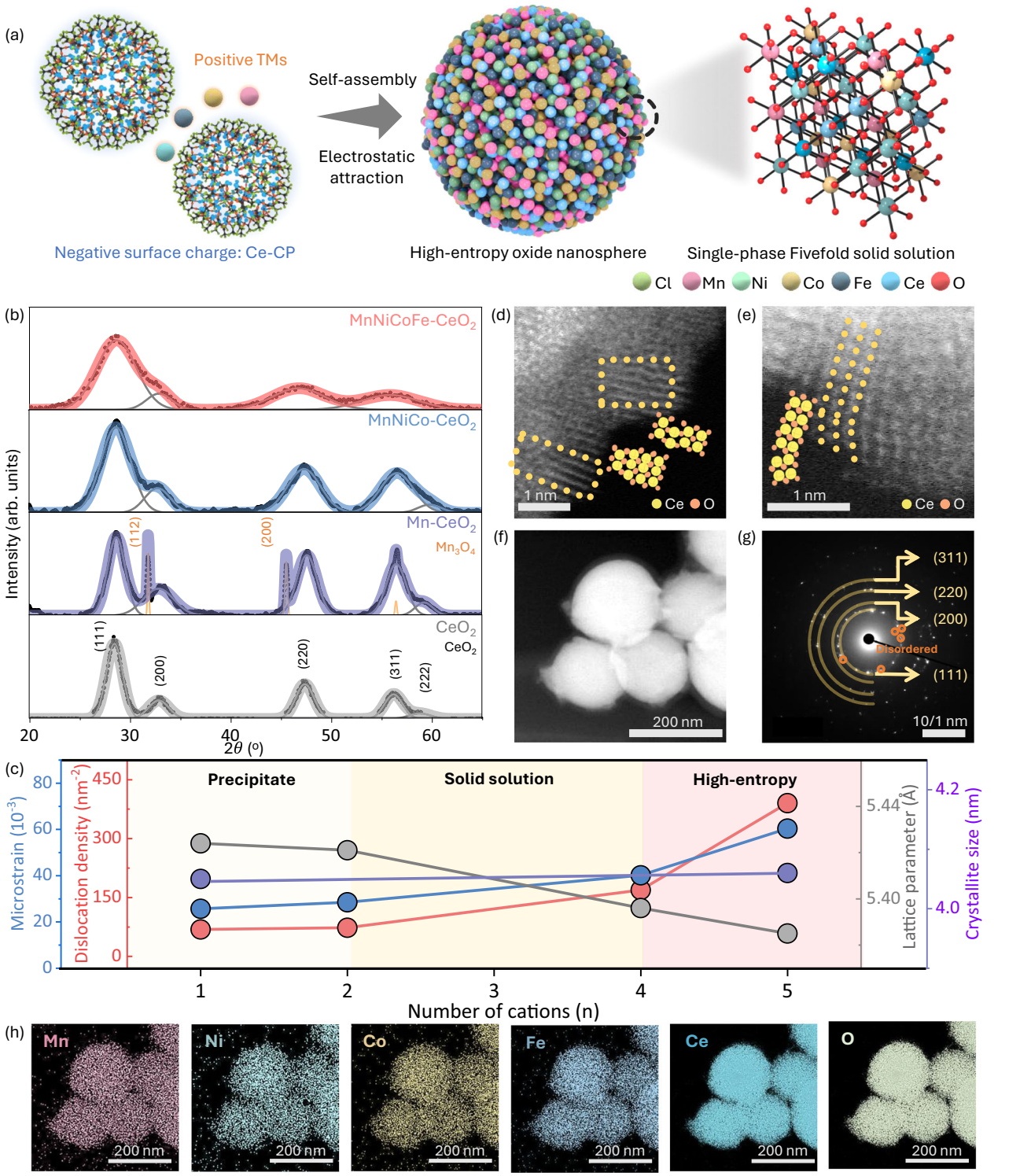

Fig. 1 | Structural and compositional characterization of disordered ceria-based oxides. a Schematic of synthesis process (TMs = transition metal ions, Ce-CP = $Ce(TCA)_2(OH)_2{\cdot}2H_2O$); **b** XRD patterns of CeO_2, Mn-CeO_2, MnNiCo-CeO_2, and MnNiCoFe-CeO_2 (intensities scaled identically); **c** comparison of XRD parameters; ADF-STEM images of 2D planar defects in MnNiCoFe-CeO_2 (scale bar: 1 nm): **d** stacking faults and twinning, **e** screw dislocation; **f** ADF-STEM image of MnNiCoFe-CeO_2; **g** SAED pattern; **h** STEM-EDS mapping of MnNiCoFe-CeO_2.

pattern (Fig. 1g), as revealed by the additional dots (representing disordered states) in the proximity of single-phase concentric rings. Several unusual types of 2D planar defects (Fig. 1d, e) appear, supporting the conclusion of a high extent of structural disorder and correspondingly improved reactivity. The morphology of MnNiCoFe-CeO_2, showing spherically shaped particles (Fig. 1f, Supplementary Fig. 3), with a homogeneous distribution of all elements (Fig. 1h), combined with XRD and SAED results, indicate the formation of a homogeneous solid solution. MnNiCoFe-CeO_2 exhibits the highest defect density in laser Raman microspectroscopy (Supplementary Fig. 4), as evidenced by the maximal defect concentration of 51.7%. This observation, combined with the absence of TM-O bonding

https://doi.org/10.1038/s41467-026-69849-4

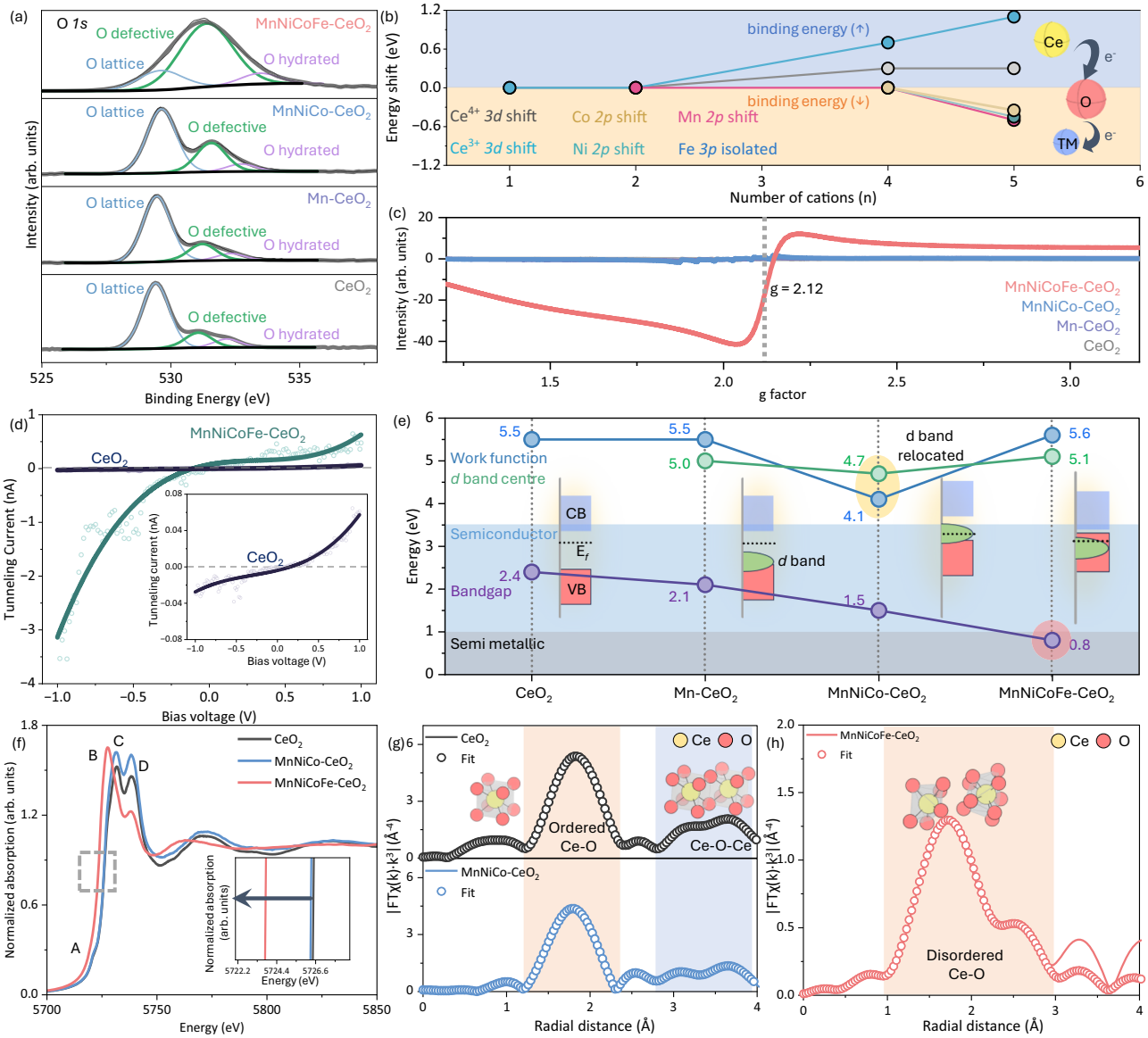

Fig. 2 | Chemical and electronic structure characterization of disordered ceria-based oxides. a XPS O*1s* orbital (intensities scaled identically); **b** XPS data summary (TM = transition metals); **c** EPR spectra; **d** IV curve; **e** electronic band structure summary (VB = valance band, E_f = Fermi level, CB = conduction band); **f** normalized Ce L_3-edge XANES spectra; Fourier-transforms of K^3-weighted Ce L_3-edge EXAFS spectra and corresponding fitting results for: **g** CeO_2 and MnNiCo-CeO_2, **h** MnNiCoFe-CeO_2.

features in the Raman spectra, confirms the presence of significant structural disorder and the maintenance of a single-phase structure of the Ce-O framework in the HEO state. The high defect concentration is indicative of a high frequency of oxygen vacancies, as evidenced by the 605 cm^{-1} Raman peak intensity. This high concentration of oxygen vacancies is likely to cause clustering in order to lower the total elastic energy of the system[24]. Such clustered vacancies are likely to be responsible for the formation of extended 2D structural defects, including the observed stacking faults, twin boundaries, and dislocations, which disrupt the oxygen sublattice[25,26]. These findings also provide a possible explanation for the apparent mismatch between surface-sensitive techniques, such as XPS, and bulk-sensitive techniques, such as Raman. While XPS may underestimate the extent of defect formation due to its shallow probe depth, the 2D defects identified by HADDF for the material surface offer direct evidence of surface-localized oxygen sublattice distortion, thereby aligning with the XPS- and Raman-based observations.

For a deeper understanding of defects contributing to structural disorder in HEOs, it is essential to explore the alteration in the nature of the chemical bonding. Surface-chemical analysis by X-ray photoelectron spectroscopy (XPS) is used to determine not only surface valence changes of elements but also the chemical bonding alteration[27]. The oxygen environment serves as a reliable indicator of the behavior of different cations as oxygen acts as the direct bridge between them. The deconvoluted O *1s* spectra (Fig. 2a) reveals constant oxygen defect concentration in CeO_2 (19%) and Mn-CeO_2 (~20%) based on the relative areal proportions of the O-lattice (529 eV), and O-defective (531 eV) peaks[28], suggesting unchanged metal-oxygen bonding and the high stability of the oxygen-sublattice. With increasing solid solution complexity (MnNiCo-CeO_2), there is a small increase in O-defective/O-lattice ratio (22%) (Supplementary Fig. 5), suggesting that the addition of Ni and Co facilitates the formation of a small amount of oxygen vacancies, which are classified as point defects[29]. These individual oxygen vacancies may introduce localized disruptions in the lattice, but they are limited to a minor effect. However, a significant

enhancement in the O-defective/O-lattice ratio (up to 85%) is observed in MnNiCoFe-CeO_2. This reveals that the defects in the HEO are not limited to point effect (individual oxygen vacancies) but suggests that the oxygen vacancies are clustered, which would correspond to significant destabilization of the oxygen-sublattice in forming the 2D defect illustrated in Fig. 1d, e. This dramatic increase highlights that the addition of the fifth element fundamentally alters the defect dynamics in the HEOs. This phenomenon induces a significant transformation in the oxygen environment, resulting in the destabilization of the oxygen sublattice. This destabilization is likely driven by multivalence charge transfer (MVCT)[30,31] which amplifies the effects of multiple metal ions simultaneously interacting with oxygen ions. This collective interaction reduces the intrinsic metal-oxygen bonding affinity, destabilizing the oxygen sublattice and forming 2D defects, thus causing the structural disorder.

Electronic disorder

The phenomenon of MVCT[31] in HEOs equates to the presence of electronic disorder. Therefore, the distinctive effect of each cation on the charge transfer can be elucidated through analysis of their chemical bonding alteration, as revealed through the deconvolution and comparison of the *3d*, *2p*, and *3p* XPS spectra for CeO_2, Mn-CeO_2, MnNiCo-CeO_2, and MnNiCoFe-CeO_2 (Supplementary Fig. 5). The Ce$3d_{5/2}$ spectrum of CeO_2 shows two different Ce chemical environments, with the presence of Ce^{4+} (882.2 eV, 888.7 eV, and 898.2 eV) and Ce^{3+} (880.3 eV and 884.1 eV)[28]. In Mn-CeO_2, the Ce^{3+} and Ce^{4+} XPS binding energies are unchanged, suggesting retention of the original Ce chemical environments after the addition of Mn (Fig. 2b). However, in MnNiCo-CeO_2, the binding energies of Ce^{3+} and Ce^{4+} are increased, indicating that the addition of Ni and Co cause electronic interactions within the Ce environment. These interactions result in alterations to the Ce-O bond, which can be attributed to the formation of a solid solution. The addition of Ni and Co also promotes the Ce-O bond to a state of enhanced ionicity, reflecting a significant modification in the bonding nature. These changes are likely driven by the smaller crystal radii and higher electronegativities of Ni and Co compared to those of Ce^{4+} and Ce^{3+}, thereby encouraging electron transfer toward the Ni and Co sites (Supplementary Fig. 6,7 and Table 4). The addition of Fe in MnNiCoFe-CeO_2 induces a further increase in the binding energy of Ce^{3+} but no noticeable effect on Ce^{4+}. This shift for Ce^{3+} is likely due to the higher electronegativity of Fe^{3+} (1.556, Supplementary Table 4) compared to that of Ce^{3+} (1.348). Since both of these closely associated ions share the same valence state, this suggests a reason for the fixed valence state of Fe. However, the electronegativity of Ce^{4+} (Ce^{4+} = 1.608) is very close to that of Fe^{3+}, confirming that little shift in binding energy for Ce^{4+} would be expected. In MnNiCoFe-CeO_2, the binding energies of Mn, Ni, and Co exhibit lower binding energies, indicating distortions in the TM-O bonds. Therefore, the overall lattice distortion in MnNiCoFe-CeO_2 is likely to reflect the cumulative result of distortions occurring in both the Ce-O and TM-O bonds. These shifts also suggest an increase in TM-O bond covalency, underscoring the alteration of the structural order in the HEO relative to that of the less complex solid solutions. The importance of the alteration of the chemical environment and the resultant improvement in charge-transfer phenomena is supported by the multiple charge-transfer permutations between the four TMs and Ce of the HEO, although the Fe shows only one stable valence as confirmed by Supplementary Table 5 and Fig. 8.

The observed improvement in charge-transfer phenomena suggests a corresponding alteration in the electronic structure of HEOs. To gain deeper insights into these changes, quantitative electron paramagnetic resonance (EPR) spectroscopy was employed to investigate the distribution and behavior of unpaired electrons. Variations in signal intensity, line shapes, and *g*-factors provide valuable insights into the redistribution of electron density and the nature of electronic interactions within the HEO lattice[32,33]. The three less-complex solid solutions display multiple low-intensity hyperfine (Supplementary Fig. 9), indicating a limited number of unpaired electrons in the lattice, likely trapped at point defect sites such as oxygen vacancies[34]. However, MnNiCoFe-CeO_2 exhibits a prominent, isolated peak, indicating a significantly higher proportion of unpaired electrons within the HEO in Fig. 2c. Notably, the contributions of the three-dimensional *g*-factors (g_x, g_y, g_z) become nearly equal[32], reflecting a transition to an isotropic and electron-rich environment in the HEO, suggesting a high degree of electronic disorder. The differentiation of the *g*-factors allows the identification of lattice-localized electrons (*g*-factor <2.003) and surface delocalized electrons (*g*-factor >2.003)[32]. The highest peak intensity (*g*-factor = 2.120) indicates that substantial proportions of the unpaired electrons are surface-delocalized. This delocalization is likely to be a key factor in providing high electronic conductivity, enabling efficient charge transport. The asymmetric EPR signal is indicative of a Dysonian nature, which arises owing to a skin effect and microwave penetration in materials with appreciable electrical conductivity, such as metallic or semimetallic systems[35,36]. This asymmetry serves as strong evidence that the material has undergone a transition from semiconducting to more conductive behavior associated with a high extent of electronic disorder, which is facilitated by partial reduction, a high concentration of oxygen vacancies, and mixed-valence states. In such systems, unpaired electron spins can become delocalized or interact with conduction electrons, further contributing to the Dysonian response and enhanced signal intensity. The high concentration of delocalized electrons present in the HEO can enable them to interact with reactive species, thereby enhancing the material's ability to adsorb and desorb oxygen species efficiently. The presence of a high concentration of delocalized electrons is supported further by photoluminescence spectra for MnNiCoFe-CeO_2 (Supplementary Fig. 9), which show low recombination extents, which are consistent with high electron mobility and transport, thus representing the delocalized state. The direct evidence for a transformation into an electron-rich environment with high electronic conductivity in the HEO is demonstrated by the 100-fold increase in tunneling current density (from −30 pA in CeO_2 to −3 nA at the bias voltage at −1 V), as shown in Fig. 2d. Such high current tunneling in MnNiCoFe-CeO_2 indicates highly conductivity and efficient charge transport[37]. This effectively metallic conductivity, which is attributed to a greatly increased electron means free path and electronic disorder, also represents optimized electron transfer in the HEO, which provides a crucial advantage for catalytic and electrochemical reactions.

The detailed electronic structure was analyzed further in order to understand the electronic transfer behavior shown in Fig. 2e and Supplementary Figs 10–12. CeO_2 shows general semiconducting features, with a bandgap of 2.4 eV and work function (WF) of 5.5 eV. Mn-CeO_2 shows a band gap slightly reduced to 2.1 eV, without any change to the WF. MnNiCo-CeO_2 exhibits a further decrease in the band gap to 1.5 eV, but the WF changes to lower value, accompanied by a downward shift in the position of the *d*-band center. The position of the *d*-band center, determined through VB-UPS, is indicative of the material's tendency to adsorb molecules on transition metal sites during catalytic and electrochemical reactions[38]. These shifts in both the WF and *d*-band center suggest slight electronic disorder and rearrangement of the *d*-band position above the Fermi level, leading to potential benefits in the catalytic processes and air battery performance as they facilitate the respective adsorption and desorption of reactants and products, thus improving overall reaction kinetics. In MnNiCoFe-CeO_2, the WF and the *d*-band center return to their original positions as observed in CeO_2. However, an intriguing change is observed in the band gap, which decreases significantly to ~0.75 eV. This reduction indicates a high extent of electronic disorder and a transition towards semimetallic properties[39], which directly correlates with the enhanced electronic conductivity. The distinction in band structures for MnNiCo-CeO_2 and MnNiCoFe-CeO_2 suggests that these materials

facilitate different electronic disorder and electrocatalytic reaction mechanisms. In MnNiCo-CeO_2, the electronic structure is slightly altered with low *d*-band position, which can reduce the activation energy for the adsorption of reactive species; in MnNiCoFe-CeO_2, the electronic structure is highly disordered by transformation from the original semiconducting to semimetallic properties with enhanced electronic conductivity from the narrow band gap, leading to the promotion of more rapid charge transfer processes.

For an in-depth understanding of the electronic disorder at the atomic scale, the X-ray absorption near-edge structure (XANES) spectra of the Ce L_3-edge were examined. The four observed white-line peaks associated with the electronic structure of Ce in CeO_2 (5720–5760 eV)[40–42] were subjected to Gaussian mode fitting (Fig. 2f, Supplementary Fig. 13, and Supplementary Table 6). Pre-edge peak A is associated with the final states of the Ce 5*d* orbitals at the bottom of the conduction band. Peak B arises from a dipole-induced transition of Ce 2*p* electrons to the Ce $4f^{1}5d$ final state, which involves an extra electron in the Ce 4*f* orbital (associated with Ce^{3+}). Peak C represents charge transfer from the Ce $4f^{1}5d$ final state of Ce to the O 2*p* orbital of the ligand. Peak D is attributed to a different final state configuration (associated with Ce^{4+}), which is the $4f^{0}5d$ state. The deconvolutions reveal that CeO_2 and MnNiCo-CeO_2 are similar in that they exhibit the typical local structure of CeO_2, as evidenced by the consistency of the integrated peak areas for all four peaks and the greater intensities of peaks C and D relative to those of A and B (Supplementary Table 3). In contrast, the shifts from CeO_2 and MnNiCo-CeO_2 to MnNiCoFe-CeO_2 demonstrate an increase in the integrated B peak area and a decrease in that for peak C. These results for MnNiCoFe-CeO_2 are consistent with increasing electron delocalization in the Ce 4*f* orbital (associated with Ce^{3+}) and decreasing delocalization of the electrons in the O 2*p* orbital of the ligand. Thus, the increase in the net disorder of the HEO is apparent. On the other hand, Peak D is consistent in its lower intensity for MnNiCoFe-CeO_2 relative to those of CeO_2 and MnNiCo-CeO_2. Since this decrease is consistent with a decrease in [Ce^{4+}] and a complementary increase in [Ce^{3+}] (as shown by with the observed increased B peak area), then the addition of a fifth metal indicates a further increase in electron disorder deriving from the additional charge transfer between Ce and this metal. The inset of Fig. 2f reveals a minor leftward shift in the absorption edge for MnNiCo-CeO_2 compared to that of CeO_2, indicating that the incorporation of Mn, Ni, and Co induces only a relatively small change in the electron transfer between these metals and Ce and thus the $Ce^{4+} \leftrightarrow Ce^{3+}$ redox. In contrast, the shift for MnNiCoFe-CeO_2 is significantly greater, which again is consistent with increased electron disorder deriving from the additional charge transfer between Ce and the fifth metal.

The observation for the Ce site in XANES contradicts that for the Ce site in the XPS spectra of the HEO. While the peak shifts in XPS suggest electron transfer from Ce toward the TM sites, both the XANES and XPS data indicate an increase in the relative concentration of Ce^{3+}. This seemingly contradictory result can be explained by considering the electronic nature of Ce[43]. Owing to the delocalized Ce free electrons (as shown by the band structure analysis and CAFM), Ce can donate electrons from the Ce conduction band to both the neighboring transition metals (as shown by XPS data) and the Ce^{3+} state associated with the 4*f* electron orbital (as shown by XANES data). Thus, both the electron transfer and increase in [Ce^{3+}] can occur simultaneously. In addition, the large formation of oxygen vacancies provides the necessary charge compensation at the Ce sites, as confirmed by Raman, EPR, and XPS data, further stabilizing the reduced Ce^{3+} state despite the electron transfer from Ce toward the TMs.

Atomic disorder

Extended X-ray absorption fine structure (EXAFS) results show the local Ce-O bond environment, which can reveal changes at the atomic scale. The phase-uncorrected Fourier transform EXAFS (FT-EXAFS) data for CeO_2 (Fig. 2g, Supplementary Fig. 14, and Supplementary Table 7) show that CeO_2 exhibits bond lengths of 2.34 Å (Ce-O) and 4.27 Å (Ce-O-Ce), which match those of the cubic structure (2.37 Å and 4.30 Å, respectively), with a coordination number (CN) of 8[42,44]. MnNiCo-CeO_2 (Fig. 2g) shows a slight decrease in the respective bond lengths (2.30 Å and 4.21 Å) and a reduction in the CN to 7.47, indicating minor bond and lattice distortion. These changes are likely to be consistent with the formation of individual oxygen vacancies. In contrast, MnNiCoFe-CeO_2 (Fig. 2h) six different Ce-O bond lengths (2.19 and 2.24 Å [contracted] and 2.44, 2.53, 2.61, and 2.87 Å [expanded]) and a low CN of 6.10. These significant alterations in the Ce lattice demonstrate the conversion of eight equidistant bonds to six irregularly disordered bonds and a correspondingly significant decrease in the crystal symmetry, which are indicative of significant atomic disorders. The formation of low-CN disordered Ce centers renders the Ce sites unsaturated, which can provide empty coordination positions capable of binding reactive molecules such as OH^- and O_2. This can result because unsaturated sites have an innate tendency to achieve maximal coordination. This phenomenon suggests that low-CN disordered Ce centers can serve as pivotal active sites in electrocatalytic processes, including electrocatalytic OER/ORR reactions in air battery systems. Further, the marked reduction in Ce–O–Ce bond intensity signifies a disruption in the long-range order[44,45], suggesting that Ce atoms are randomly dispersed throughout the crystal lattice (as evidenced by element occupancy analysis (Supplementary Table 3 and HR-HAADF atomic-line profiles in Supplementary Fig. 15). This randomness suggests that a high extent of atomic disorder and the resultant active sites are not only in close proximity, but they also are distributed randomly within the lattice, thus having the potential to enhance the overall catalytic performance by providing abundant and readily accessible sites for electrochemical reactions.

The atomic disorder and lattice distortion in Fig. 3a, which reflect structural asymmetry, are indicated by the highly irregular interionic angles. The inter-plane angle along [111] and [100] zone axes in MnNiCoFe-CeO_2 are fully disordered, shifting to 52° to 112° from the ideal respective angles of 60° and 90° (Fig. 3b–d)[46]. This lattice distortion probably derives largely from the mixed substitutional-interstitial solid solubility of all of the transition metal ions in the matrix phase, as revealed by the XRD refinement (Supplementary Table 3 and Fig. 1), ADF-STEM images (Supplementary Fig. 15), and related defect equilibria, the latter of which support the charge-compensation basis for the formation of oxygen vacancies and free electrons (Supplementary Table 8).

In order to assess the impact of the electronic environment induced by the TMs on the atomic disorder and performance of the HEO, linear scans of the electron energy loss spectroscopy (EELS) spectra were done on the TMs within an HEO crystal. Detailed analyses of the atomic surface effects also were done since catalytic reactions occur predominantly at the surface (Fig. 3e–i and Supplementary Fig. 16). The matrix Ce $M_{4,5}$-edges indicate electron transitions from the Ce$3d_{3/2}$ (Ce M_4) and Ce$3d_{5/2}$ (Ce M_5) core levels to the Ce*4f* unoccupied electronic states[47]. From the bulk to the surface, the disappearance of the M_5 satellite peaks and the increased M_5:M_4 intensity ratio indicate a reduction for Ce^{4+} to Ce^{3+}, implying a high density of surface *f*-electrons and subsequent surface reactivity[47]. Further, the positive shift in the M_5 peak energy from bulk to surface suggests an altered surface Ce electronic environment. The respective 3*d* TM (Mn, Ni, Co, and Fe) states exhibit an L_2-edge ($2p_{1/2}$ to unoccupied *3d*) and an L_3-edge ($2p_{3/2}$ to unoccupied *3d*), the differences between which were analyzed through the $L_{2,3}$-edge energy loss difference (ΔE) (Supplementary Tables 9–12)[48]. Surface-specific ΔE and L_2-edge shift changes were observed for Mn, Ni, and Fe, indicating enhanced charge-transfer dynamics and modification of the electronic environment (influenced by changes in oxidation state, coordination number, bond length, and associated defect generation)[49]. In contrast, Co exhibited minimal ΔE

https://doi.org/10.1038/s41467-026-69849-4

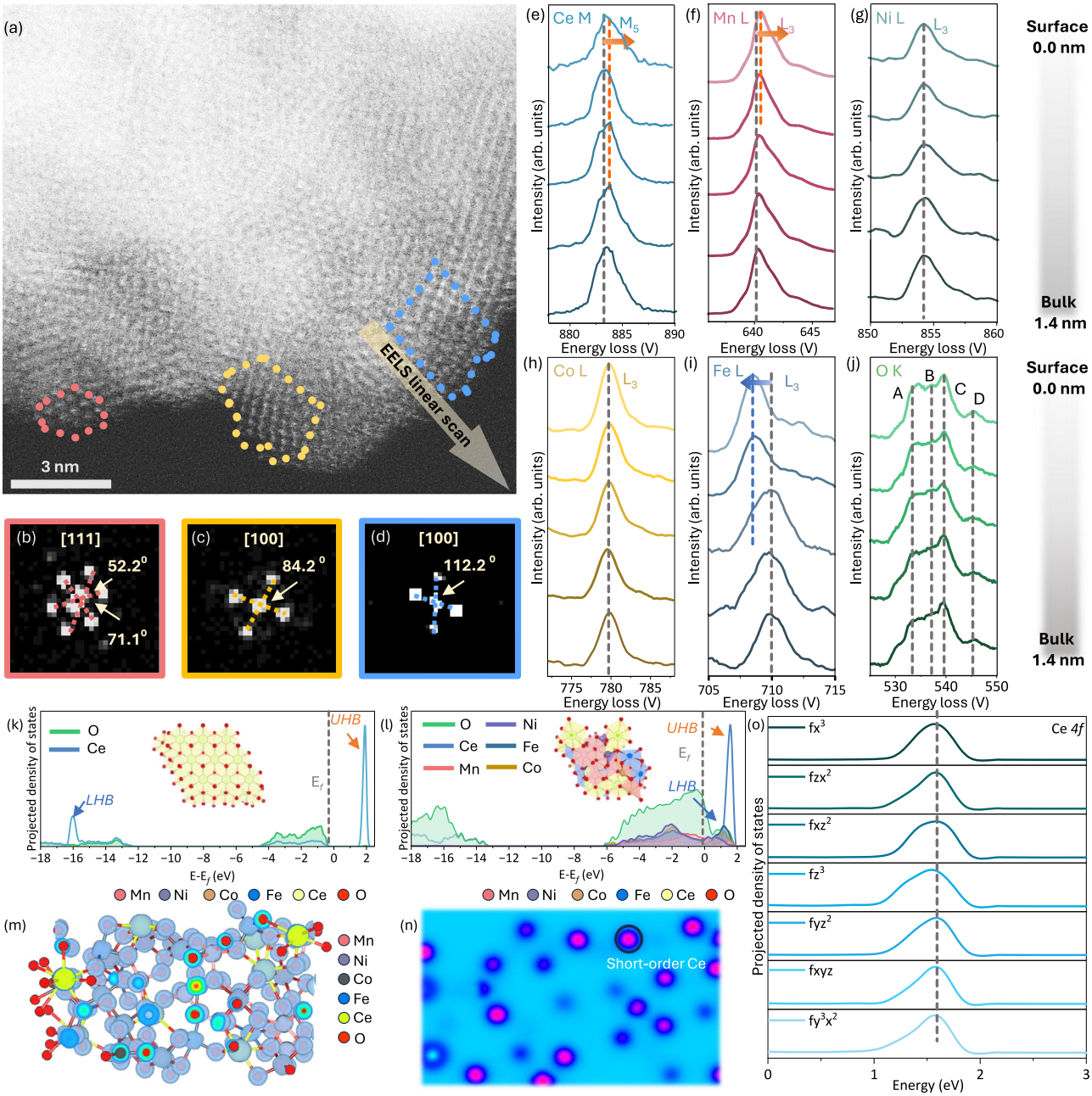

Fig. 3 | Atomic-scale structural and electronic structure analyses of multilevel-disordered MnNiCoFe-CeO2. a AC-HAADF image; Corresponding FFT patterns for single-crystal regions: **b** red outlined area, **c** yellow outlined area; **d** blue outlined areas; EELS spectra for linear scans: **e** Ce M-edge, **f** Mn L-edge, **g** Ni L-edge, **h** Co L-edge, **i** Fe L-edge, **j** O K-edge; Electronic structure analyses: **k** PDOS for CeO_2 (LHB = lower Hubbard band, UHB = upper Hubbard band), **l** PDOS for MnNiCoFe-CeO_2, **m** ELF of (311) plane; **n** charge-density differences (blue perimeter = electron density) of (111) plane; Corresponding orbital-projected states: **o** Ce*4f* states.

variation or L_2-edge shift changes, suggesting a more passive electronic role, likely contributing to structural and electronic stability within the HEO matrix. The O K-edge (Fig. 3j) reveals distinct peaks (A, B, C) that correspond to electronic hybridization between O*2p* states and the unoccupied *3d* or *4f* states of metals orbitals, while peak D represents the cubic structural framework[50]. The broadened and partial degeneration of all peaks is consistent with variable extents of atomic disorder from bulk-to-surface.

An in-depth understanding of the electronic structure can be gained by analysis of the projected density of states (PDOS), as shown in Fig. 3k, l. The pristine CeO_2 shows generic semiconductor features such that the Ce4*f* domain is located on the conduction band; this feature also is identified as the upper Hubbard band (UHB); both of these correspond to the Ce4f^0 to Ce4f^1 electronic transition[51]. The O2*p* domain is located at the valence band with slight Ce4*f*-O2*p* hybridization, suggesting the strong ionic and weak covalent bonding nature of CeO_2[52]. The lower Hubbard band (LHB) is a critical feature used to determine the lowest ionization potential of metal ions. In the case of CeO_2, the LHB is observed at a relatively high energy level of approximately −16 eV, indicating a deeply localized electronic state. This positioning suggests that the Ce^{4+} ions in CeO_2 exhibit a strong affinity to retain their electrons, making it energetically unfavorable to adsorb oxygen effectively during catalytic reactions. The MnNiCoFe-CeO_2 (Supplementary data 1) exhibits a significantly different electronic behavior compared to pristine CeO_2, characterized by the absence of a band gap. This indicates a transition to a semimetallic

state, as seen in Fig. 3l. The semimetallic nature of MnNiCoFe-CeO_2 is illustrated further by the approximately equal DOS of the TMs near the Fermi energy level (Fig. 3i and Supplementary Fig. 17). This balanced contribution from the TMs near the Fermi level suggests a high density of free electrons, which underpins increased electronic conductivity.

The electron localization function (ELF) and charge density difference plots (Fig. 3m, n and Supplementary Fig. 18) imply the electron densities of atoms. As shown in Fig. 3n, m and Supplementary Figs. 18 and 19, the interactions between the Ce-O bonds and Co, Ni, Fe, and Mn exhibit relatively high electron densities, indicating a clear redistribution of electronic charge from Ce to the TMs. Further, the oxygen ions that bridge the high-CN Ce and TMs show lower electron densities relative to those arising from those that bridge low-CN Ce and TMs. These data again propose the role of the greater amount of charge transfer and resultant increased electron disorder associated with the low-CN Ce relative to that of the high-CN Ce. It is counter-intuitive for there to be a higher electron density of the low-CN Ce, which would be expected to be lower owing to the undercoordination. This apparent contradiction is heightened in light of the differential electronegativities of Ce, where the higher value for a higher Ce^{4+}/Ce^{3+} ratio of high-CN Ce would be expected to exhibit a higher electron density compared to that for the lower Ce^{4+}/Ce^{3+} ratio of low-CN Ce. The low-CN Ce would result in highly catalytically reactive sites that would facilitate the adsorption and the subsequent reduction of O_2 molecules. The asymmetry of the densities of states of Ce 4*f* shown in Fig. 3o further supports the critical importance of the alteration of charge transfer and electron disorder associated with the HEO.

OER/ORR performance and kinetics

A fundamental understanding of the operational mechanism of HEOs in OER (charging) and ORR (discharging) is essential to the design of high-performance and efficient cathodes in ZABs. Figure 4 and Supplementary Fig. 21 show electrocatalysis data for OER and ORR performances, each measured in triplicate to ensure reproducibility, with corresponding error bars included to indicate experimental variability. As shown in Fig. 4a–c and Supplementary Table 13, the OER activity was evaluated using three key metrics: (1) overpotential at 10 mA cm^{-2} (representing onset OER performance), (2) overpotential at 50 mA cm^{-2} (reflecting high-rate performance), and (3) Tafel slope (indicating reaction kinetics). Stoichiometric single-phase CeO_2 exhibited poor performance, demonstrating inferior onset OER performance, high-rate capability, and sluggish kinetics. In contrast, Mn-CeO_2, which forms a dual-phase mineralogy, showed similarly poor onset OER performance but moderately improved high-rate capability and OER kinetics. These data suggest that, while the intrinsic activity is limited, the formation of heterojunctions could enhance charge transport, albeit at the risk of blocking active sites. Further improvement was observed in the homogeneous solid solution catalysts MnNiFe-CeO_2 and MnNiCo-CeO_2. These systems displayed small onset performance and average high-rate capability and OER kinetics, which are attributed to the introduction of slight structural disorder in the form of point defects and individual charge-compensating oxygen vacancies (which act as additional adsorption sites at low oxygen vacancy concentrations ($[V_{\ddot{O}}]$). Additionally, slight electronic disorder (*d*-band relocation and enhanced charge transfer) was found to optimize the binding energy of the reaction intermediates[53], further improving intrinsic activity and reaction kinetics. Importantly, the similar OER preformation between MnNiFe-CeO_2 and MnNiCo-CeO_2 reveals that the improved OER performance is not due to the presence of only Fe, a known active-site element[54], but rather the overall increase in material complexity and disorder. Of all of the catalysts examined, the high-entropy oxide MnNiCoFe-CeO_2 demonstrated the most significant enhancement, outperforming even the commercial benchmark IrO_2 in onset OER performance, high-rate capability, and OER kinetics. As shown in Supplementary Fig. 20, despite the Ni (common active site in OER as well) in the MnNiCoFe-CeO_2 HEO, no distinct Ni oxidation peak was observed during CV or LSV measurements[55]. This absence indicates that Ni does not serve as an active redox center in the OER process. Instead, it is likely to play a synergistic assisting role, contributing to the modulation of the local electronic environment through MVCT, thereby enhancing overall conductivity and structural stability. This conclusion is supported further by the subsequently presented XANES data and DFT simulations, both of which confirm that Ni does not participate directly in discrete redox transitions under OER conditions but rather supports the activity of the active metal centers.

A similar trend is observed in the ORR performance. Three metrics were used to evaluate the activity: (1) half-wave potential, which reflects the intrinsic ORR activity; (2) diffusion-limited current density, which reflects the mass transport capability; and (3) Tafel slope, which indicates the ORR kinetics from Fig. 4d–f and Supplementary Fig. 22. Pristine CeO_2 exhibits inferior ORR activity, with average mass transport and kinetics, consistent with its known limitations as a stoichiometric single-phase material. Mn-CeO_2 shows a moderate improvement in ORR activity, although both mass transport and ORR kinetics are reduced. These data suggest that the biphasic system behaves differently in ORR compared to that in OER. The improvement in activity may stem from the presence of Mn_3O_4 as a secondary phase, which is known to be catalytically active for ORR[56,57]. Conversely, the declines in mass transport and ORR kinetics likely result from partial blocking of O_2 gas access due to surface occlusion. MnNiFe-CeO_2 and MnNiCo-CeO_2 catalysts display similar average ORR performances, mass transports, and ORR kinetics. These results suggest that these specific dopant combinations produce only incremental effects on the activity. Nevertheless, the presence of slight structural and electronic disorder appears to influence positively the ORR performance, consistent with the benefits observed in the OER process. Notably, the high-entropy oxide MnNiCoFe-CeO_2 demonstrates great ORR activity, mass transport, and ORR kinetics. Although it does not match the benchmark performance of commercial Pt/C catalysts in terms of half-wave potential, it achieves comparable mass transport capability and even better ORR kinetics. This further confirms that the great activity and efficiency of MnNiCoFe-CeO_2 is not attributable to the simple additive effects of individual metal dopants, as shown in the electron transfer numbers of MnNiCoFe-CeO_2 > MnNiCo-CeO_2 ≈ MnNiFe-CeO_2 > Mn-CeO_2 > CeO_2 in Supplementary Fig. 23. Instead, it arises from the multilevel disorder, structural, electronic, and atomic, which collectively gives rise to highly active, catalytic sites and improved electronic transport properties.

This enhanced activity in OER and ORR is explained by comparison between the two types of solid solutions. For the example MnNiCo-CeO_2, the existence of 0D point defect formation, low dislocation density, and low microstrain equate to a relatively low extent of lattice distortion (structural disorder). MnNiCo-CeO_2 exhibited limited-valence-state charge transfer (four permutations – $Mn^{2/3+}$, Ni^{2+}, Co^{2+}, $Ce^{3/4+}$), semiconducting behavior (electronic disorder), low [Ce^{3+}], and eightfold Ce coordination (atomic disorder). In contrast, for MnNiCoFe-CeO_2, there were 2D defect formation (additional adsorption sites in the form of stacking faults, twin boundaries, and dislocations, which result from the formation of what are likely to be associated oriented oxygen vacancy clusters (high $[V_{\ddot{O}}]$) associated with the high [Ce^{3+}]), high dislocation density, and high microstrain. This exhibited enhanced multiple-valence-state charge transfer (sixteen permutations – $Mn^{2/3+}$, $Ni^{2/3+}$, $Co^{2/3+}$, Fe^{3+} $Ce^{3/4+}$), semimetallic behavior (thus enhancing electron transport), high [Ce^{3+}], and ~sixfold Ce coordination (which acts as active site).

For further investigation of the electrochemical behavior of MnNiCoFe-CeO_2, the Koutecky-Levich curves (Fig. 4g and Supplementary Figs. 24,25) denote that this HEO system favors a four-electron reduction pathway (the same as Pt/C), with no by-product

https://doi.org/10.1038/s41467-026-69849-4

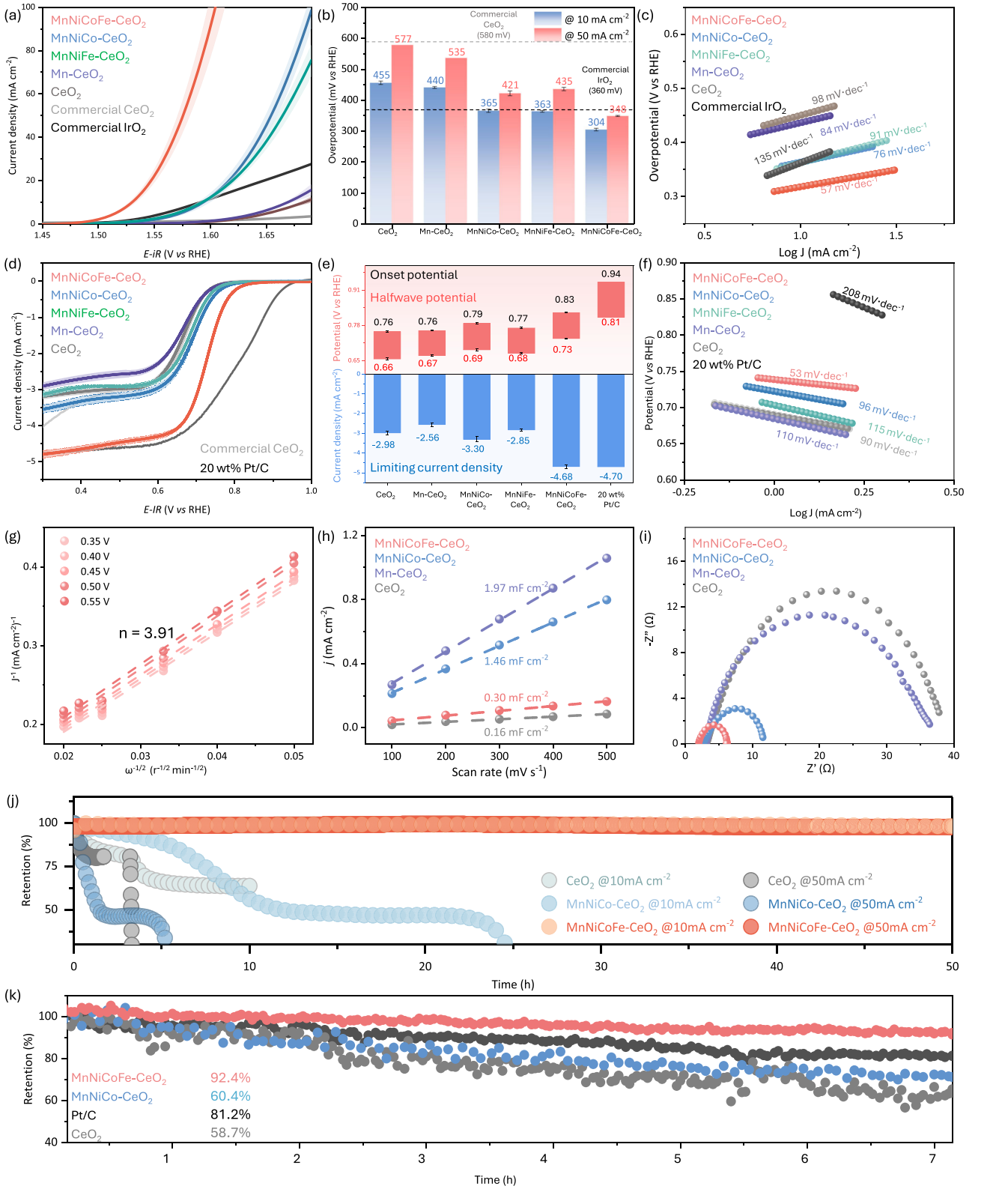

Fig. 4 | Bifunctional OER/ORR electrocatalytic performance of ceria-based oxides. OER performance (at 1.0 M KOH, pH = 14.0 ± 0.1; room temperature, loading mass = 0.5 mg cm^{-2}): **a** LSV curves (scan rate = 5 mV/s, the resistance of the solution was 1.4 ± 0.1 Ω, shaded regions indicative of error bars for triplicate measurement); **b** overpotentials; **c** Tafel plots; ORR performance (at 0.1 M KOH, pH = 13.0 ± 0.1, loading mass = 0.2 mg cm^{-2}, room temperature): **d** LSV curves (scan rate = 5 mV/s, rotation rate = 1600 rpm, the resistance of the solution was 43.2 ± 2.1 Ω, shaded regions indicative of error bars for triplicate measurement); **e** onset potentials, halfwave potentials, limiting current densities; **f** Tafel plots; Electrochemical characterization: **g** K-L plots; **h** ECSA plots; **i** Nyquist plot stability testing; stability tests: **j** OER stability testing; **k**ORR stability testing.

formation, demonstrating that the HEO has highly efficient electron transfer and adequate binding energies for oxygen atoms. The low electrochemical surface area of MnNiCoFe-CeO_2 (Fig. 4h and Supplementary Fig. 26) highlights the necessity of maximal disordering of the structure through alteration of the bond nature to maximize the intrinsic electrocatalytic activity in HEOs. The Nyquist plot (Fig. 4i) reveals low electrical and ionic resistances in MnNiCoFe-CeO_2, confirming the catalytic benefits of its semimetallic electrical conductivity and highly disordered lattice. Moreover, the HEO shows stable long-term performance in both OER and ORR. The OER stabilities of CeO_2, MnNiCo-CeO_2, and MnNiCoFe-CeO_2 were evaluated under both low (10 mA cm^{-2}) and high (50 mA cm^{-2}) current densities (Fig. 4j). The CeO_2 rapidly lost activity, decreasing by ~40% within ~10 h at 10 mA cm^{-2}, completely losing activity within only ~3 h at 50 mA cm^{-2}, revealing its poor durability under intense operating conditions. MnNiCo-CeO_2 exhibited great stability, maintaining ~50% activity for ~24 h at 10 mA cm^{-2}, although it also failed within ~6 h at 50 mA cm^{-2}. In contrast, the MnNiCoFe-CeO_2 demonstrated great long-term stability, retaining ~98% of its initial activity for ~50 h at both 10 mA cm^{-2} and 50 mA cm^{-2}. This high stability is attributed to electronic disorder in the multiple charge-transfer permutations between the Ce and four TMs of the HEO, which have the potential to homogenize the bulk charge transfer and hence electrical conductivity.

More to the point, this homogenization would reduce the differential field and valence effects imposed during the extended mean free path of electron transfer, as suggested in Fig. 2d. More generally, the increased configurational entropy would result in decreased Gibbs free energy and hence chemical stability. These considerations apply to the preceding OER data but also to ORR data, where again the homogeneous nanostructure of HEO outperformed the composite microstructure of benchmark Pt/C (Fig. 4k and Supplementary Fig. 27). This optimized charge transfer and low Gibbs free energy state explain the great long-term stability of the HEO catalyst compared to commercial Pt/C. Although the HEO exhibits a slightly lower electron transfer number than the composite Pt/C, this difference can be attributed to the intrinsic nature of the materials. The Pt/C composite generally possesses higher Gibbs free energy from mixed phases and charge trapping at heterogeneous interfaces, which can compromise long-term electrochemical stability. In contrast, the HEO, as a well-mixed single-phase solid solution, minimizes interfacial charge trapping and provides a more stable energy landscape. The Pt/C composite system shows a higher apparent electron transfer number, likely due to its greater selectivity toward the four-electron ORR pathway.

Active site characteristics

Examination of the stability of the multilevel disorder at different time scales is essential to understand the operational and degradation mechanisms of HEOs during catalytic reactions, as shown in Fig. 5a. The *structural stability* of the HEO in terms of OER and ORR after activation and extended testing was analyzed by Raman. As shown in Fig. 5b, no additional peaks appeared after activation, indicating that the Ce-O framework remains the dominant active phase. Even after long-term cycling, the Raman spectra remain unchanged, further confirming the high structural stability of the HEO and the absence of TM-containing secondary phase, which are observed commonly to result from TM diffusion, hydroxylation, and/or oxidation[58,59]. This stabilization is facilitated by the large extent of lattice distortion as a form of stress relief. Further, the relatively small changes in the oxygen defect concentrations in the HEO of <13% (shifting from the initial 51.7 to 45.8–58.2%; Fig. 5) confirm this stability. The *electronic stability* was assessed by EPR spectroscopy, as shown in Supplementary Fig. 28, where the decreases in the *g*-values immediately after OER and ORR activation indicate temporary electron localization, probably associated with OH^- or O_2 adsorption at active sites. However, after long-term cycling, the *g*-values returned to their original states and no signal splitting was observed, confirming reversible and stable electronic disorder behavior. The *atomic stability* of the HEO was evaluated by EDS mapping of pristine and post-reaction HEOs (Supplementary Fig. 29). These data confirm the maintenance of elemental homogeneity in the absence of volumetric segregation, thus supporting compositional consistency under operating conditions.

The identification, evolution, and stability of the active sites were examined by ex situ XANES and EXAFS analyses of Mn, Ni, Co, Fe, and Ce at different time stages (initial, post-activation, post-testing, and long-term)[60]. These data elucidate the oxidation state changes, coordination environment evolution, and role of multi cation interactions in sustaining catalytic activity and stability. In order to evaluate the behavior of the TMs during catalysis, the Mn, Ni, Co, and Fe K-edges were examined. Both the XANES and EXAFS spectra show only minor variations in Fig. 5c and Supplementary Fig. 30, confirming that the TMs undergo minimal changes under operating conditions. The charge-transfer dynamics revealed by the XANES data allow differentiation of the contributions of the individual TMs to the OER and ORR in Fig. 5c[61]. Ni and Fe show more positive edge shifts during OER, indicating their greater participation in oxygen evolution. In contrast, Mn and Co exhibit more negative edge shifts during ORR, suggesting their greater involvement in oxygen reduction. These minor yet distinct contributions suggest that Mn and Co act as auxiliary facilitators during ORR, whereas Ni and Fe assist during OER, while Ce is the dominant active center. The EXAFS analysis of the TMs also confirms only subtle modifications in the local coordination environments, indicating that they are not active sites. Detailed inspection of the EXAFS data (Supplementary Fig. 30) reveals that all four TMs experienced small increases in M-O coordination after activation (upward trajectory), consistent with limited oxygen adsorption[58,59]. Over extended cycling, the first coordination sphere exhibits a slight decrease (downward trajectory, though still above pre-testing levels), which probably reflects the role of individual point defects. In contrast, the second coordination sphere exhibits a slight increase (upward trajectory), which is consistent with modest M-O-M ordering of the lattice after long-term testing[58,59].

In the case of Ce, more pronounced spectral shifts in XANES were observed during OER and ORR processes, indicating electron-transfer processes associated with Ce sites, as shown in Fig. 5d. The distinct shift in the Ce L_3-edge after OER, compared to that after ORR, suggests that Ce plays fundamentally different roles in the two reactions. The oxidation of Ce active sites is attributed to their direct participation in OER by the $Ce^{3+} \rightarrow Ce^{4+}$ transition, highlighting that OER has a stronger impact on the Ce oxidation state. Such redox transitions likely facilitate Ce-OH bond formation. Both post-testing and long-term stability measurements reveal further oxidation of the Ce sites, indicating that Ce oxidation plays an important role in OER activation. In contrast, the absence of a significant shift after ORR suggests a more passive role, where Ce sites act primarily as adsorption centers for O_2 molecules, without notable changes in oxidation state. The data for XANES over long-term cycling confirm that Ce largely retains its original electronic configuration, thus reflecting its high atomic stability.

The local atomic coordination of Ce, which was characterized by EXAFS, further illustrates the distinct behavior of the Ce-O bonds during OER (Fig. 5e) and ORR (Fig. 5f). After OER activation, the disordered Ce-O bond structure is preserved although the overall intensity increases suggest higher Ce coordination while maintaining the bonding types (both ordered Ce-O and disordered Ce-O) of the initial HEO. Increasing the coordination of the Ce is indicative of OH^- bonding at the Ce center, confirming the role of Ce as the active site. After 10 h, the Ce-O bonds display a positive shift, which confirms structural alteration and bond elongation, consistent with the upward trajectory observed during stability testing. After long-term OER cycling, the Ce-O bonds return to their initial state, thus retaining the bonding characteristics of the initial HEO and confirming that local

https://doi.org/10.1038/s41467-026-69849-4

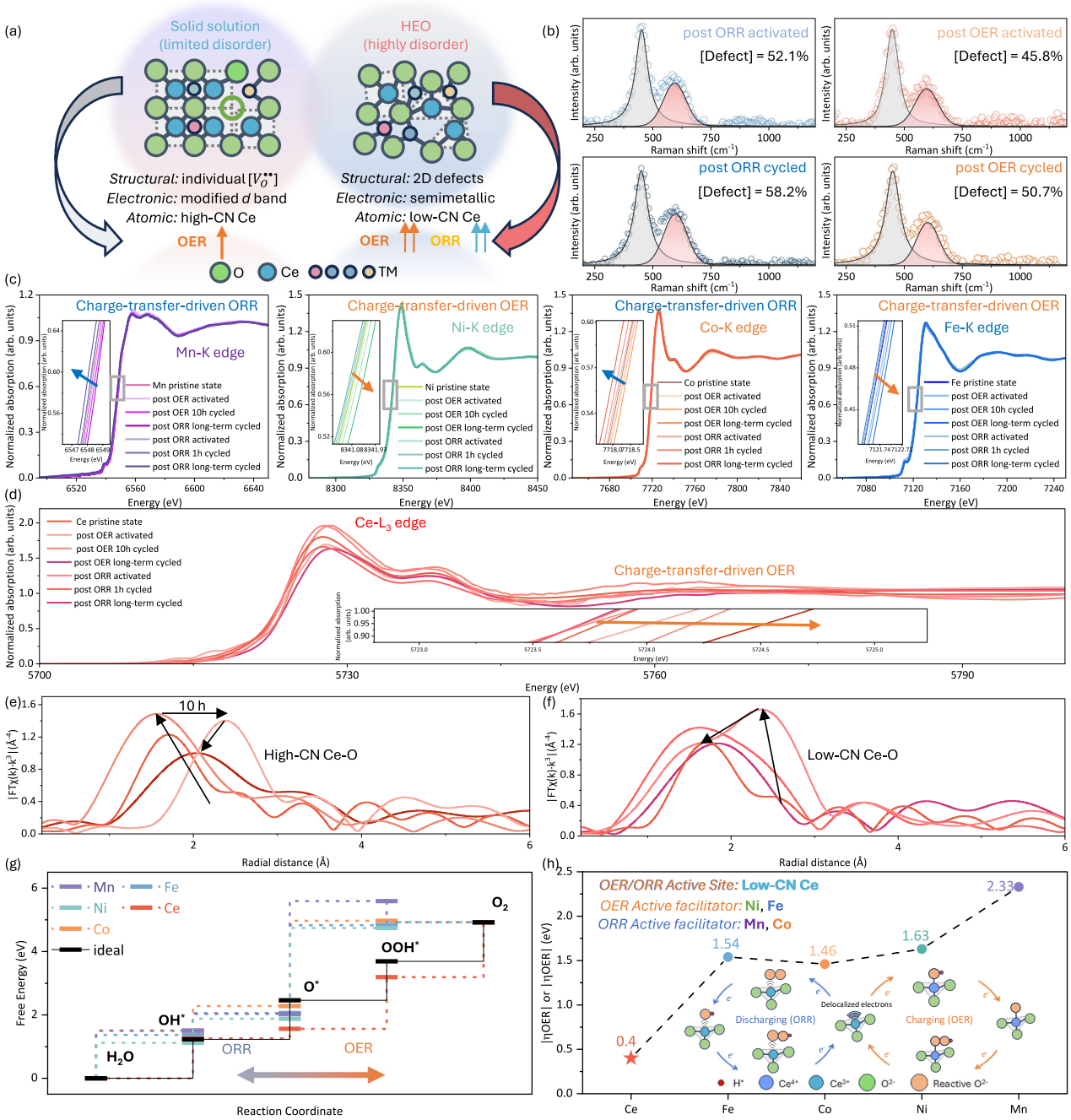

Fig. 5 | Active-site characterization and mechanism analysis of multilevel disordered HEO in OER/ORR process. Ex situ OER and ORR at different times scales: **a** schematic of effect of multilevel disorder engineering; **b** laser Raman microspectra; **c** normalized Mn-K, Ni-K, Co-K, and Fe-K edge XANES spectra; **d** normalized Ce-L_3 edge XANES spectra; **e** OER (Fourier-transform of K^3-weighted Ce L_3-edge EXAFS spectra), **f** ORR (Fourier-transform of K^3-weighted Ce L_3-edge EXAFS spectra); **g** calculated ORR/OER free energy diagrams; **h** calculated ORR/OER overpotential of each element.

structural degradation is not significant under OER conditions. In contrast, Ce active sites behave differently in ORR. After activation, the ordered Ce-O bonds remain largely unchanged while the intensity of the disordered Ce-O bonds increases, where the latter suggests weak Ce-O_2 interactions that promote O_2 adsorption and reduction, confirming that Ce is the active site for ORR. However, after extended ORR testing and long-term operation, the amount of disordered Ce-O bonds diminishes, thereby increasing the proportion of ordered Ce-O bonds. This effectively decreases the dynamic flexibility of the Ce-O bonds, thus leading to electron localization at the Ce sites and reducing the availability of delocalized electrons required for efficient O_2 adsorption and dissociation during ORR. Together, these findings demonstrate that Ce defect sites act as crucial active centers, playing distinct roles in OER and ORR: in OER, they participate directly through redox cycling and bond reconstruction while, in ORR, they function mainly as adsorption centers.

In order to identify which of the metal constituents are the active sites in the high-entropy oxide, both OER and ORR pathways, each involving four electron transfer steps, were analyzed using first-principles DFT simulations, as shown in Fig. 5g. Optimized surface models were constructed for each metal ion site (Mn, Ni, Co, Fe, Ce), with adsorption energies calculated for all key oxygenic intermediates

(*OH, *O, *OOH) along the reaction pathways. Of all the sites, Ce ions exhibited the lowest energy barriers across the reaction steps, suggesting that these are the primary active sites. For Ce, the rate-determining step is the formation of *OOH, with the largest free energy barrier (ΔG) of 1.63 eV. Similar trends were observed for other metal sites but with higher energy barriers for *OOH formation. The calculated overpotentials of Mn, Ni, Co, Fe, and Ce are used to represent the overall OER/ORR activity of these metal ions in Fig. 5h, aligning the dominance of Ce (only 0.4 eV) with the experimental activity trend. These findings suggest the pivotal role of low-CN Ce sites in facilitating both OER and ORR processes, while the other transition metals primarily play supportive roles, as also confirmed by the EXAFS data.

TMs commonly are identified as active sites in OER and ORR reactions[62,63]. However, in the present work, they have been shown not to serve as the primary active centers. This difference is explained in terms of multilevel disorder engineering in high-entropy oxides. (1) *Structural disorder:* A large number of oxygen vacancies are formed, and these preferentially localize and cluster around Ce owing to its flexible Ce^{3+}/Ce^{4+} redox couple and the low energy barrier for vacancy formation. This reduces the likelihood of TM participation in reactions with active oxygen intermediates. (2) *Electronic disorder:* The semimetallic nature of the HEO, combined with the presence of multiple cations, induces strong electronic disorder (*d*-band broadening and shifting). This *bridging* effect suppresses the distinct localized redox activity of individual TMs, thereby reducing any catalytic contribution and, instead, acting primarily as charge-transfer mediators rather than distinct active sites. (3) *Atomic disorder:* EXAFS analysis shows that, in HEOs, TMs typically are locked into high-CN frameworks with limited distortion. This structural rigidity further reduces their ability to participate directly in catalytic reactions. Together, these factors explain why, unlike in conventional catalysts, the TMs in this HEO system do not act as dominant active sites, with Ce defect centers' instead playing the primary catalytic role.

Promising Zn-air battery performance

The rechargeable ZAB was assembled by coupling the MnNiCoFe-CeO_2 as cathode with a pure Zn plate as anode (Fig. 6a). The discharge stage of the ZAB was powered by the ORR on the catalyst surface and stripping Zn^{2+} from the anode, while the cell was charged through the OER coupling with the Zn^{2+} plating. The battery with MnNiCoFe-CeO_2 shows an open circuit voltage of 1.461 V while the one with benchmark Pt/C + IrO_2 displays a lower voltage of 1.424 V, as shown in Fig. 6b. The MnNiCoFe-CeO_2 ZAB yields a high specific capacity of 739.6 mAh g_{Zn}^{-1}, with a stable discharge plateau of 1.19 V at a current density of 5 mA cm^{-2} (Fig. 6c). This capacity was calculated according to the consumption of the Zn anode, which was ~90% of the theoretical capacity of Zn (824 mAh g^{-1}), thus verifying the promising performance of the assembled ZAB. The MnNiCoFe-CeO_2 ZAB delivers promising peak power density of 162.7 mW cm^{-2}, which is much higher than that of the benchmark IrO_2 + Pt/C (127.5 mW cm^{-2}), as shown in Fig. 6d. Further, the MnNiCoFe-CeO_2 catalyst also displays stable rate capacity, maintaining higher discharge voltages at current densities from 2 mA cm^{-2} to 40 mA cm^{-2} and good voltage retention compared to the Pt/C+IrO_2 benchmark electrode (Fig. 6e). The resultant chemical stability and catalytic activity of MnNiCoFe-CeO_2 supports its cycling stability of the ZABs, exhibiting stable operation over 450 h at a current density of 5 mA cm^{-2}, while the benchmark Pt/C + IrO_2 lasts only for <100 h (Fig. 6f). The ZAB also exhibits reduced overpotentials (0.7 *vs* 1.0 V), with constantly higher discharge plateaux and lower charge voltages (inset of Fig. 6f), demonstrating the promising catalytic performance of MnNiCoFe-CeO_2. More importantly, the spike at the end of the stability testing suggests an unknown associated effect on the anode, confirmed by the Zn anode's being fully corroded after the long-term test, as shown in Supplementary Fig. 31. Thus, a more stable zinc anode could be expected to result in the prolongation of the cycling stability of this type of ZAB. Further examination of the impact of degradation of the cathode was done using XANES and EXAFS analyses, as shown in Supplementary Fig. 32. These data reveal that the electronic configuration and low CN of Ce are stable, so deterioration of the cathode is not the principal cause battery failure. This overall combination of notable performance and long-term stability reveals MnNiCoFe-CeO_2 to be the top promising cathode for ZABs, as confirmed in Supplementary Table 15.

These findings of promising performance of MnNiCoFe-CeO_2 in ZABs highlight the critical importance of multilevel disorder engineering in HEOs, as shown in Fig. 6g. In the single-phase oxide of minimal disorder, the electrochemical performance is poor. In the dual-phase heterojunction, the electrochemical performance is just slightly enhanced by this effect. In the lower-complexity solid solutions, the degree of structural disorder is limited, where there are isolated point defects and individual charge-compensating oxygen vacancies that provide only a small number of active adsorption sites. The modest lattice distortion helps to maintain a coherent lattice framework with minimal internal strain. Electronic disorder still retains the semiconducting properties, but with *d*-band relocation's modifying the binding energy of the reaction intermediates, while the mixed-valence states of the metals enhance charge transfer to a commensurately limited extent. However, the largely unchanged atomic disorder contributes little to catalytic improvement.

In contrast, the highly disordered HEO leverages the board synergy between structural, electronic, and atomic disorders, thereby significantly enhancing the electrocatalytic activity. The structural disorder is manifested as 2D defects; including stacking faults, twin boundaries, and dislocations; which are associated with oxygen vacancy clusters. These defects offer additional adsorption sites while preventing long-range ordering or phase segregation, thereby enhancing single-phase stability during cycling. The electronic disorder is evidenced by semimetallic behavior, which promotes high electronic conductivity and facilitates multivalence charge transfer across sixteen redox permutations (*e.g.*, $Mn^{2+}/^{4+}$, $Ni^{2+}/^{3+}$, $Co^{2+}/^{3+}$, Fe^{3+}, $Ce^{3+}/^{4+}$), allowing the potential for all cations to contribute cooperatively, as evidenced by the XANES data in Fig. 5c, d. Finally, the atomic disorder introduces a higher fraction of Ce^{3+} and low-coordination Ce, that latter of which is the active site that enhances the OER/ORR performance further, as shown in Supplementary Table 13, and leads to the promising ZAB performance and stability, as shown in Supplementary Table 15. Further, this multilevel disorder engineering suggests a fundamental roadmap for the design of materials, paving the way for sustainable energy solutions.

Methods

Chemicals and materials

All metal salts [$Ce(NO_3)_6{\cdot}6H_2O$ (99.00%) and $MnCl_2$, $NiCl_2$, $CoCl_2$, and $FeCl_3$ (99.95%)] as well as NaOH and ethanol (≥ 99.00%) were from Sigma-Aldrich (Sydney, Australia). Trichloroacetic acid (TCA, Cl_3CCOOH, ≥99.00%) was sourced from Chem-Supply Pty Ltd. (Sydney, Australia). Experiments employed a standard three-electrode arrangement: FTO-coated glass served as the working electrode (Wuhan Geao Scientific Education Instrument, Wuhan, China; sheet resistance ~21 Ω square^{-1}), a Pt plate (4 cm^2) was used as the counter electrode, and an Ag/AgCl electrode (BASi Inc., Evansville, IN, USA) provided the reference. Before measurements, the FTO electrode was sequentially sonicated in acetone, ethanol, and DI water for 5 min per step.

Synthesis of Ce-CP rod precursors

Chronopotentiometric deposition was performed using an electrochemical workstation (Ezstat Pro; 300 μV potential resolution and 3 nA current resolution in the ±100 μA range) together with the three-electrode configuration described above. Fresh electrolyte was

https://doi.org/10.1038/s41467-026-69849-4

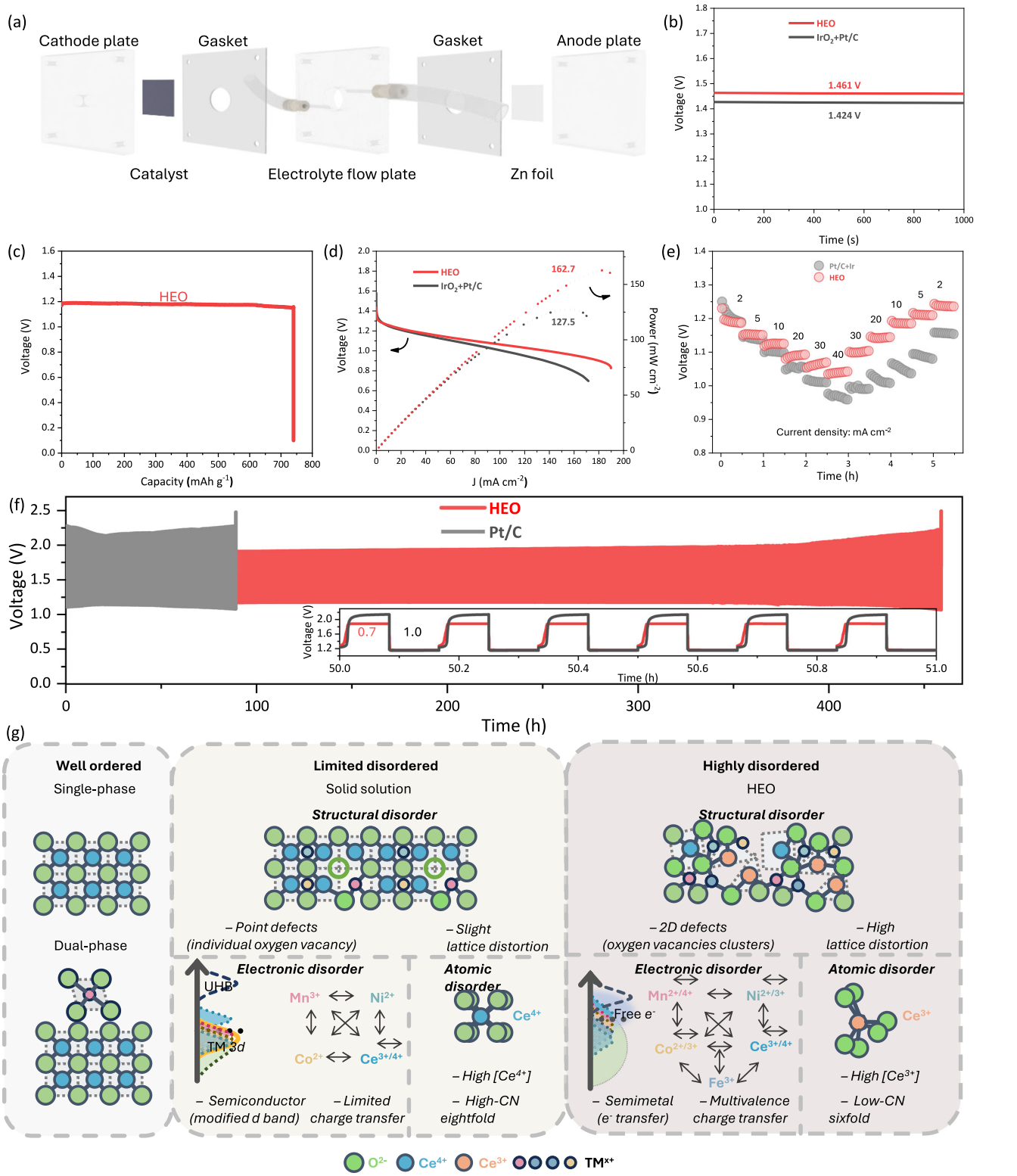

Fig. 6 | Rechargeable Zn–air battery performance and durability of multilevel-disordered HEO cathodes compared with Pt/C + IrO2 benchmarks. a Schematic illustration of construction of ZAB (at 6.0 M KOH + 0.2 M $Zn(Ac)_2$, room temperature); **b** OCP curves; **c** specific capacity test curve for HEO; **d** power density curves; **e** rate capabilities at different rates from 2 to 40 mA cm^{-2} and back to 2 mA cm^{-2}; **f** long-term cycling performances at charging/discharging rate of 5 mA cm^{-2} (5 min charge and 5 min discharge); **g** schematic of multilevel disorder in HEO for high performance ZABs.

prepared immediately before each experiment by dissolving trichloroacetic acid (0.05 M) and $Ce(NO_3)_3{\cdot}6H_2O$ (0.05 M) in deionized water and making up the volume to 150 mL. The solution pH was then brought to 6.2 ± 0.1 by titration with 1 M NaOH (pH 14.0 ± 0.1). The electrolyte was transferred to glass bottles and kept at ambient conditions until use. Deposition was conducted galvanostatically at 30 mA over an FTO working area of 15 cm^2, which provided uniform films while maintaining a high growth rate.

Synthesis of Ce-CP derived CeO_2

To synthesize the CeO_2, Ce-CP (300 mg) precursor was dispersed in 300 mL bipolar medium (DI water:ethanol volume ratio: 1:1 v/v) and mixed for 20 min at 400 rpm. The resultant solution was dried at 80 °C in air for 12 h. The NaOH aqueous solution (0.15 M) was added for oxidation and mixed for 5 h. The resultant suspensions were centrifuged at 2800 × *g* for 10 min, followed by resuspension in DI water and centrifuging additional three times. The samples then were reduction annealed at 400 °C for 4 h in forming gas (5% H_2 + 95% Ar; heating rate 3 °C/min). The resultant CeO_2 powders were stored in sealed containers prior to characterization and testing.

Synthesis of TMO high-entropy oxide

The TMO-based high entropy oxide was synthesized using an identical procedure to that for CeO_2 powders except that the TM salts (8 mol% per each element, metal basis) were added to the solution containing the Ce-CP when the bipolar medium was formed.

Characterization

Powder XRD patterns were recorded using a Philips X Pert multipurpose diffractometer with Cu Kα radiation (45 kV, 40 mA), using a step size of 100.00° in 2θ and a scan rate of 0.2° min^{-1} (2θ). Diffraction peaks were processed in X Pert HighScore Plus. High-resolution TEM (HRTEM), selected-area electron diffraction (SAED), and EDS measurements were carried out on a JEOL JEM-F200 S/TEM operated at 200 kV. Surface morphology and compositional mapping by SEM/EDS were performed using an FEI Nova NanoSEM in both primary and secondary electron imaging modes, with an accelerating voltage of 10–15 kV. ADF-STEM imaging and EELS analyses were conducted on a JEOL JEM-GrandARM300F2 double aberration-corrected STEM (AC-STEM) operated at 300 kV. ADF-STEM data were recorded using a 200 mm camera length, corresponding to inner and outer collection angles of 32 and 175 mrad, respectively. EELS spectra were acquired using a Gatan GIF Continuum spectrometer equipped with a K3 single-electron detector. For EELS acquisition, a 2 cm camera length and a 32 mrad convergence angle were applied, together with an EELS entrance aperture of 108 mrad. The energy resolution was determined from the FWHM of the zero-loss peak (ΔE_{ZLP} = 0.54 eV), and spectra were collected with a dispersion of 0.18 eV per channel. The EELS energy axis was corrected to compensate for ZLP drift and background subtraction was performed using power-law fitting. Raman microspectroscopy was performed on a Renishaw inVia confocal Raman microscope equipped with a helium–neon green laser and a 1800 grooves mm^{-1} grating. Spectra were collected from 100 to 1500 cm^{-1} with 1 cm^{-1} resolution (laser power 35 mW; spot diameter ~2 µm). Data handling used Renishaw WiRE 4.4, and spectral positions were calibrated using the Si band near 520 cm^{-1}. XPS and UPS were acquired on a Thermo Fisher Scientific ESCALAB 250Xi system using a monochromated Al Kα source (1486.6 eV) and a hemispherical analyzer. During measurements, the analysis chamber pressure was maintained below 0.8–1.0 kPa. Binding energies were referenced to the C *1s* peak set to 285 eV. Peak fitting employed mixed Gaussian–Lorentzian line shapes, and spectra were normalized to minimize contributions from adventitious carbon (C *1s* at 285–286 eV). Conductive AFM (CAFM) was performed with a Bruker AFM platform. Local current–voltage (I–V) responses were measured using a PtIr-coated conductive probe to assess nanoscale electrical conductivity. X-ray absorption fine structure (XAFS) measurements were collected at the XAFCA beamline (Australian Synchrotron, Melbourne) at the Mn, Ni, Co, and Fe K-edges and the Ce LIII-edge. Post-cycled samples of the Ce LIII-edge XAFS data was carried out using easyXAFS. Spectra were processed in Athena, including linear-combination fitting (LCF), and EXAFS modeling was completed in Artemis (Demeter XAS suite). EXAFS signals were obtained following background removal and normalization, k^3-weighting, and fast Fourier transformation (FFT) of the XAS data.mmPhotoluminescence (PL) spectra were obtained at room temperature using a Shimadzu RF-5301PC spectrofluorophotometer with 325 nm excitation. EPR measurements were performed on a Bruker EMX X-band ESR spectrometer operating at 9.8 GHz; spectra were recorded with a center field of 3200 mT modulation amplitude of 4 G, and microwave power of 0.6325 mW, and were processed in Bruker Xenon. Diffuse reflectance UV–Vis–NIR spectra were measured using a PerkinElmer Lambda 1050 double-beam spectrophotometer equipped with a triple-detector configuration, across 200–1500 nm. The indirect optical band gap was estimated using the Kubelka–Munk transformation.

Electrochemical oxygen evolution reaction characterization

Catalyst inks were formulated by dispersing 5 mg of the catalyst in 0.5 mL of a 1:1 (v/v) ethanol/DI-water mixture, then adding 25 µL of Nafion solution (Sigma-Aldrich, 99.99%) as a binder. The dispersion was ultrasonicated until fully uniform. The resulting ink was drop-cast onto Teflon-treated carbon-fiber paper (1 × 1 cm^2) to prepare the working electrode, giving a mass loading of 0.5 mg cm^{-2}. A 1.0 M KOH electrolyte (pH 14.0 ± 0.1) was prepared by dissolving 28.06 g KOH in deionized water and diluting to 0.50 L in a volumetric flask; the solution was stored in a PTFE bottle at 25 °C. Electrochemical measurements were carried out in this electrolyte using a three-electrode configuration comprised of the catalyst-coated carbon paper working electrode, a graphite rod counter electrode, and a Hg/HgO reference electrode. The Hg/HgO reference was calibrated against a reversible hydrogen electrode (RHE) in 1.0 M KOH using a Pt wire working electrode under hydrogen-saturated conditions (high-purity H_2). All experiments were conducted at 25 °C and ambient pressure with a CHI 760E electrochemical workstation. Measured potentials were corrected for ohmic losses using 85% IR compensation and are reported versus RHE, calculated according to: E_{RHE} (V) = $E_{Hg/HgO}$ (V) + 0.098 + 0.059 × pH. Cyclic voltammetry (CV) and electrochemical impedance spectroscopy (EIS) were performed in the same 1.0 M KOH solution. EIS spectra were recorded at 1.3 V vs RHE from 100 kHz to 0.1 Hz using a 10 mV a.c. amplitude, and the solution resistance was obtained from impedance analysis. The electrochemically active surface area (ECSA) was estimated from the double-layer capacitance (C_{dl}) by collecting CVs in a non-Faradaic potential window (0.98–1.08 V vs RHE) at several scan rates; C_{dl} was taken from the slope of capacitive current versus scan rate. ECSA was then calculated using. ECSA = C_{dl}/C_s, with a specific capacitance C_s = 60 µF cm^{-2}. Durability toward OER was assessed galvanostatically in 1.0 M KOH for 50 h at two current densities (10 and 50 mA cm^{-2}).

Electrochemical oxygen reduction reaction characterization

The electrolyte 0.1 M KOH (pH = 13.0 ± 0.1) was prepared by dissolving 5.61 g KOH pellets in deionized water, diluting to 1 L in a volumetric flask, thoroughly mixing, transferring to a PTFE bottle, and storing at 25 °C. Test electrodes were prepared by drop-casting 10 µL of an ink made by ultrasonically blending 2.5 mg catalyst, 2.5 mg Ketjen Black 300 J, 50 µL 5 wt% Nafion, and 950 µL isopropanol, giving 25 µg catalyst per electrode (loading = 0.2 mg cm^{-2}) on a polished glassy carbon rotating disk electrode (RDE, Pine Research Instrumentation) or a rotating ring-disk electrode (RRDE, Pine Research Instrumentation) followed by drying in air (geometric area, A = 0.125 cm^2). Electrochemical measurements were performed, collected, and analyzed in a standard three-compartment cell (0.1 M KOH in all compartments) on a CHI 760E workstation using a glassy carbon working electrode, a graphite rod counter electrode, and an Hg/HgO reference electrode; data were acquired with the CHI software and processed offline. The Hg/HgO reference was calibrated vs RHE in H_2-saturated 0.1 M KOH at 25 °C using a Pt wire, and all potentials were IR-compensated at 85% and converted to the RHE scale using E_{RHE} (V) = $E_{Hg/HgO}$ (V) + 0.098 + 0.059 × pH. The solution resistance was determined

through EIS analysis. CV tests were conducted in nitrogen- and oxygen-saturated 0.1 M KOH electrolyte at room temperature, which assessed the catalytic properties of the materials. The tests employed a scan rate of 50 mV/s within a voltage range of 0.05 to 1.1 V. Linear sweep voltammetry (LSV) curves were obtained in an oxygen-saturated 0.1 M KOH solution, which was tested at a sweep rate of 5 mV/s and various rotation speeds in the range 400-2500 rpm. In order to ensure that the electrolyte was fully saturated with oxygen, pure oxygen (99.999%) was bubbled into the solutions for 20 minutes before each measurement, with the flow's continuing during testing. The hydrogen peroxide yield (H_2O_2%) was calculated as follows: $H_2O_2\% = 200\ Ir\ N|Id| + Ir$, where N is the current collection efficiency of the Pt ring (37%), Ir is the ring current, and Id is the disk current of the rotating-ring disk electrode (RRDE). The electron transfer number, n, was calculated as follows: $n = 4\,|Id|/(|Id| + (Ir/N))$. Chronoamperometry (CA) was applied in order to assess the durability of the different catalysts toward ORR in 0.1 M KOH O_2-saturated electrolyte at the potential of 0.7 V.

Zn-air battery assembly

All ZAB measurements were performed using a custom-made flow-type Zn–air cell, in which the catholyte was continuously circulated through the battery chamber (cell structure illustrated in Fig. 6a). The zinc anode consisted of commercial zinc foil with a thickness of 50 µm. The foil was cut into circular disks with a diameter of 15 mm, followed by ultrasonic cleaning in a mixed ethanol/acetone solution for 20 min. After cleaning, the zinc foil was wiped with a dust-free cloth and air-dried prior to use. The Zn-air batteries were assembled in the form of a flow-type cell with a Zn foil (1 cm^2) as the anode, active-material-loaded carbon paper as the cathode, and a mixture of 0.2 M $Zn(Ac)_2$ (zinc acetate) and 6 M KOH as the electrolyte. Glass fiber separators (Whatman) were employed and cut into circular disks with a diameter of 18 mm before assembly. The cathode was prepared by spraying the active material dispersion using a spray gun on the hydrophobic carbon paper (12 mm diameter). The dispersion was prepared by mixing 5 mg HEO and 5 mg carbon black with 100 µL Nafion (5%) in 2 mL methanol. The comparison electrode was prepared through the same process using commercial Pt/C + IrO_2 as the active material. The dispersion was prepared by mixing 5 mg HEO and 5 mg carbon black with 100 µL Nafion (5%) in 2 mL methanol. The comparison electrode was prepared through the same process using commercial IrO_2 + Pt/C as the active material. The air flow was controlled by a mass flow controller (MFC). The flow rate was kept at 20 sccm. The catholyte was pumped through a peristaltic pump with a flow rate of ~30 ml/min. Compressed air was directly supplied to the cathode and regulated through the connection of the MFC. During the tests, the electrolyte was pumped continuously into the cell to ensure the smooth flow of the electrolytes in the compartments. The cathode compartment has an opening (1 cm^2) connected to an oxygen tank to allow the oxygen to flow to the cathode. All ZAB tests were conducted at room temperature (~23 °C) under ambient laboratory conditions, with a relative humidity of ~40%.

Spin-polarized density functional theory

First-principles calculations based on density functional theory (DFT)[64] were carried out using the PBEsol exchange-correlation energy functional[65] as this is implemented in the VASP software[66]. The projector-augmented wave (PAW) method[67] was employed to represent the ionic cores by considering the following electronic states as valence: Ce *5p*, *6 s*, *5 d*, *4 f*; Co 4 *s*, 3 *d*; Fe 4 *s*, 3 *d*; Mn 4 *s*, 3 *d*; Ni 4 *s*, 3 *d*; O 2 *s*, 2*p*. An energy cutoff of 650 eV and dense Monkhorst-Pack k-point grids, equivalent to 12 × 12 × 12 for the cubic fluorite unit cell containing 12 atoms, were used for integrations within the Brillouin zone, leading to total energies converged to within less than 1 meV per atom. Atomic relaxations were concluded when the forces in all of the atoms were below 0.005 eV/Å. The supercells employed for the simulation of CeO_2 and MnNiCoFe-CeO_2 surfaces included a large vacuum region of 25 Å height and a similar region of materials layers. In particular, the (111), (110), (400), (221), and (331) surface supercells contained respective totals of 243, 192, 216, 156, and 120 atoms. The *Hubbard-U* scheme, from to Dudarev et al.[68–70] was employed in the PBEsol calculations for treatment of the Ni, Fe, Co, and Mn *d* electrons and of the Ce *f* electrons, adopting respective U values of 4, 4, 4, 4, and 3 eV[68–70]. The chemically disordered systems were simulated by generating up to ten different configurations and performing averages over them. The surface formation energy, E_{surf}, was estimated using the formula: $E_{surf} = \frac{E_{DFT} - (N \cdot E_{bulk})}{2 \cdot S}$, where E_{DFT} is the energy of the slab supercell directly obtained from the DFT calculations, E_{bulk} is the energy per formula unit of the corresponding bulk system, N is the number of formula units in the surface supercell, and S is the area of the surface supercell perpendicular to the vacuum direction.

Data availability

The data generated in this study are provided in the Supplementary Information/Source Data file. Source data are provided with this paper.

References

1. Schweidler, S. et al. High-entropy materials for energy and electronic applications. *Nat. Rev. Mater.* **9**, 266–281 (2024).
2. Yao, Y. et al. High-entropy nanoparticles: Synthesis-structure-property relationships and data-driven discovery. *Science* **376**, eabn3103 (2022).
3. Kang, Y. et al. Mesoporous multimetallic nanospheres with exposed highly entropic alloy sites. *Nat. Commun.* **14**, 4182 (2023).
4. Wang, Q. et al. Fundamental comprehension, synthetic procedures and catalytic applications of high entropy oxide nanomaterials. *Mater. Today* **70**, 218–236 (2023).
5. Wang, B. et al. High-entropy phase stabilization engineering enables high-performance layered cathode for sodium-ion batteries. *Adv. Energy Mater.* **14**, 2401090 (2024).
6. Sarkar, A. et al. High-entropy oxides: Fundamental aspects and electrochemical properties. *Adv. Mater.* **31**, 1806236 (2019).
7. Wang, Q. et al. Sustainable zinc-air battery chemistry: Advances, challenges and prospects. *Chem. Soc. Rev.* **52**, 6139–6190 (2023).
8. Gao, H. et al. Revealing the potential and challenges of high-entropy layered cathodes for sodium-based energy storage. *Adv. Energy Mater.* **14**, 2304529 (2024).
9. Lu, Q. et al. Structural design of supported electrocatalysts for rechargeable Zn-air batteries. *Energy Storage Mater.* **55**, 166–192 (2023).
10. Li, L. et al. Advanced architectures of air electrodes in zinc-air batteries and hydrogen fuel cells. *Adv. Mater.* **36**, 2308326 (2024).
11. Han, N. et al. Designing oxide catalysts for oxygen electrocatalysis: Insights from mechanism to application. *Nano-Micro Lett.* **15**, 185 (2023).
12. Suntivich, J. et al. Design principles for oxygen-reduction activity on perovskite oxide catalysts for fuel cells and metal-air batteries. *Nat. Chem.* **3**, 546–550 (2011).
13. Lima, F. H. B. et al. Catalytic activity-*d*-band center correlation for the O_2 reduction reaction on platinum in alkaline solutions. *J. Phys. Chem. C.* **111**, 404–410 (2007).
14. Zheng, X. et al. Decoupling the impacts of engineering defects and band gap alignment mechanism on the catalytic performance of holey 2D CeO_{2-x}-based heterojunctions. *Adv. Funct. Mater.* **31**, 2103171 (2021).
15. Grimaud, A. et al. Activating lattice oxygen redox reactions in metal oxides to catalyse oxygen evolution. *Nat. Chem.* **9**, 457–465 (2017).
16. Xu, Y. et al. Design strategies for ceria nanomaterials: Untangling key mechanistic concepts. *Mater. Horiz.* **8**, 102–123 (2021).
17. Hsu, W. et al. Clarifying the four core effects of high-entropy materials. *Nat. Rev. Chem.* **8**, 471–485 (2024).

18. Yang, Y. et al. Rejuvenation as the origin of planar defects in the CrCoNi medium entropy alloy. *Nat. Comm.* **15**, 1402 (2024).
19. Ren, J. T. et al. High-entropy alloys in electrocatalysis: From fundamentals to applications. *Chem. Soc. Rev.* **52**, 8319–8373 (2023).
20. Pan, Y. et al. High-entropy oxides for catalysis: A diamond in the rough. *Chem. Eng. J.* **451**, 138659 (2023).
21. Guan, C. et al. The role of lattice distortion in catalysis: Functionality and distinctions from strain. *Adv. Mater.* **37**, 2501209 (2025).
22. Hu, H. et al. High-entropy engineering reinforced surface electronic states and structural defects of hierarchical metal oxides@-graphene fibers toward high-performance wearable supercapacitors. *Adv. Mater.* **36**, 2406483 (2024).
23. Mofarah, S. S. et al. Coordination polymer to atomically thin, holey, metal-oxide nanosheets for tuning band alignment. *Adv. Mater.* **31**, 1905288 (2019).
24. Esch, F. et al. Electron localization determines defect formation on ceria substrates. *Science* **309**, 752–755 (2005).
25. Eom, K. et al. Oxygen vacancy linear clustering in a perovskite oxide. *J. Phy. Chem. Lett.* **8**, 3500–3505 (2017).
26. Zheng, X. et al. Role of oxygen vacancy ordering and channel formation in tuning intercalation pseudocapacitance in Mo single-ion-implanted CeO_{2-x} nanoflakes. *ACS Appl. Mater. Inter.* **13**, 59820–59833 (2021).
27. Greczynski, G. & Hultman, L. X-ray photoelectron spectroscopy: Towards reliable binding energy referencing. *Prog. Mater. Sci.* **107**, 100591 (2020).
28. Greczynski, G. & Hultman, L. X-ray photoelectron spectroscopy: Towards reliable binding rnergy referencing. *Prog. Mater. Sci.* **107**, 100591 (2020).
29. Liao, S. et al. Engineering high-entropy duel-functional nanocatalysts with regulative oxygen vacancies for efficient overall water splitting. *Chem. Eng. J.* **471**, 144506 (2023).
30. Pastor, E. et al. Electronic defects in metal oxide photocatalysts. *Nat. Rev. Mater.* **7**, 503–521 (2022).
31. Ren, H. et al. Multivalence charge transfer in doped and codoped photocatalytic TiO_2. *Inorg. Chem.* **55**, 8071–8081 (2016).
32. Dyrek, K. & Che, M. EPR as a tool to investigate the transition metal chemistry on oxide surfaces. *Chem. Rev.* **97**, 305–332 (1997).
33. Goldfarb, D. & Stoll, S. *EPR Spectroscopy: Fundamentals and Methods*. (John Wiley & Sons, 2018).
34. Wang, Z. et al. Formation, detection, and function of oxygen vacancy in metal oxides for solar energy conversion. *Adv. Funct. Mater.* **32**, 2109503 (2022).
35. Savchenko, D. V. et al. EPR study of conduction electrons in heavily doped *n*-type 4H SiC. *Phys. Status Solidi B* **248**, 2950–2956 (2011).
36. Wang, B. et al. Electron paramagnetic resonance as A tool to determine the sodium charge storage mechanism of hard carbon. *Nat. Comm.* **15**, 3013 (2024).
37. Si, H. et al. Emerging conductive atomic force microscopy for metal halide perovskite materials and solar cells. *Adv. Energy Mater.* **10**, 1903922 (2020).
38. Wang, Z. et al. Cation-tuning induced *d*-band center modulation on Co-based spinel oxide for oxygen reduction/evolution reaction. *Angew. Chem. Int. Ed.* **134**, e202114696 (2022).
39. Grundmann, M. *Physics of Semiconductors*. Vol. 11 (Springer, 2010).
40. Paidi, V. K. et al. Role of Ce *4f* hybridization in the origin of magnetism in nanoceria. *Phy. Rev. B* **99**, 180403 (2019).
41. Marchbank, H. R. et al. Structure of nano-sized CeO_2 materials: Combined scattering and spectroscopic investigations. *ChemPhysChem* **17**, 3494–3503 (2016).
42. Ravel, B. & Newville, M. ATHENA, ARTEMIS, HEPHAESTUS: Data analysis for X-ray absorption spectroscopy using IFEFFIT. *J. Synchrotron Radi.* **12**, 537–541 (2005).
43. Wu, Y. et al. Bandwidth-control orbital-selective delocalization of *4f* electrons in epitaxial Ce films. *Nat. Comm.* **12**, 2520 (2021).
44. Fonda, E. et al. EXAFS Analysis of the L_3 Edge of Ce in CeO_2: Effects of multi-electron excitations and final-state mixed valence. *J. Synchrotron Radi.* **6**, 34–42 (1999).
45. Li, M. et al. Reinforcing Co-O covalency via Ce(*4f*)-O(*2p*)-Co(*3d*) gradient orbital coupling for high-efficiency oxygen evolution. *Adv. Mater.* **35**, 2302462 (2023).
46. Han, S. I. et al. Epitaxially strained CeO_2/Mn_3O_4 nanocrystals as an enhanced antioxidant for radioprotection. *Adv. Mater.* **32**, 2001566 (2020).
47. Garvie, L. & Buseck, P. Determination of Ce^{4+}/Ce^{3+} in electron-beam-damaged CeO_2 by electron energy-loss spectroscopy. *J. Phy. Chem. Solids* **60**, 1943–1947 (1999).
48. Pearson, D. H. et al. White lines and *d*-electron occupancies for the *3d* and *4d* transition metals. *Phys. Rev. B* **47**, 8471–8478 (1993).
49. Tan, H. et al. Oxidation state and chemical shift investigation in transition metal oxides by EELS. *Ultramicroscopy* **116**, 24–33 (2012).
50. Wu, Z. Y. et al. X-ray absorption at the oxygen k edge in cubic oxides examined using A full multiple-scattering approach. *J. Phys. Condens. Matter* **11**, 7185 (1999).
51. Huang, M. et al. Harnessing *4f* Electron Itinerancy for Integrated Dual-Band Redox Systems Boosts Lithium-Oxygen Batteries Electrocatalysis. *Angew. Chem. Int. Ed.*, e202414893 (2025).
52. Sun, Z. et al. Unlock restricted capacity via O-Ce hybridization for Li-oxygen batteries. *Adv. Mater.* **35**, 2210867 (2023).
53. Wang, X. et al. Understanding of oxygen redox in the oxygen evolution reaction. *Adv. Mater.* **34**, 2107956 (2022).
54. Anantharaj, S. et al. "The Fe Effect": A review unveiling the critical roles of Fe in enhancing OER activity of Ni and Co based catalysts. *Nano Energy* **80**, 105514 (2021).
55. Xiao, Z. et al. Exploring Ni-based alkaline OER catalysts: A comprehensive review of structures, performance, and in situ characterization methods. *DeCarbon* **7**, 100097 (2025).
56. Zhao, X. et al. Boosting ORR activity via bidirectional regulation of the electronic structure by coupling MnO/Mn_3O_4 composite materials with N-doped carbon. *ACS Sustain. Chem. Eng.* **12**, 8425–8435 (2024).
57. Bikkarolla, S. K. et al. A three-dimensional Mn_3O_4 network supported on A nitrogenated graphene electrocatalyst for efficient oxygen reduction reaction in alkaline media. *J. Mater. Chem. A* **2**, 14493–14501 (2014).
58. Zhao, Y. et al. Oxygen evolution/reduction reaction catalysts: From in situ monitoring and reaction mechanisms to rational design. *Chem. Rev.* **123**, 6257–6358 (2023).
59. Yuan, B. et al. Synergistic niobium and manganese Co-doping into RuO_2 nanocrystal enables PEM water splitting under high current. *Nat. Comm.* **16**, 4583 (2025).
60. Hao, J. et al. Unraveling the electronegativity-dominated intermediate adsorption on high-entropy alloy electrocatalysts. *Nat. Comm.* **13**, 2662 (2022).
61. Zhu, W. et al. Establishing the link between oxygen vacancy and activity enhancement in acidic water oxidation of trigonal iridium oxide. *Angew. Chem. Int. Ed.* **64**, e202423353 (2025).
62. Hou, S. et al. A review on experimental identification of active sites in model bifunctional electrocatalytic systems for oxygen reduction and evolution reactions. *ChemElectroChem* **8**, 3433–3456 (2021).
63. Chen, H. et al. Active site engineering in porous electrocatalysts. *Adv. Mater.* **32**, 2002435 (2020).
64. Cazorla, C. & Boronat, J. Simulation and understanding of atomic and molecular quantum crystals. *Rev. Mod. Phys.* **89**, 035003 (2017).
65. Perdew, J. P. et al. Restoring the density-gradient expansion for exchange in solids and surfaces. *Phys. Rev. Lett.* **100**, 136406 (2008).
66. Kresse, G. & Furthmüller, J. Efficient iterative schemes for ab initio total-energy calculations using a plane-wave basis set. *Phys. Rev. B* **54**, 11169–11186 (1996).

67. Blöchl, P. E. Projector augmented-wave method. *Phys. Rev. B* **50**, 17953–17979 (1994).
68. Menéndez, C. & Cazorla, C. Giant thermal enhancement of the electric polarization in ferrimagnetic $BiFe_{1-x}Co_xO_3$ solid solutions near room temperature. *Phys. Rev. Lett.* **125**, 117601 (2020).
69. Rahman, S. et al. Pressure-induced structural and semiconductor-semiconductor transitions in $Co_{0.5}Mg_{0.5}Cr_2O_4$. *Phys. Rev. B* **97**, 174102 (2018).
70. Cazorla, C. et al. Multiple structural transitions driven by spin-phonon couplings in A perovskite oxide. *Sci. Adv.* **3**, e1700288 (2017).

Acknowledgements

The authors are pleased to acknowledge the valuable intellectual contributions of Prof. Neeraj Sharma, School of Chemistry, UNSW Sydney. The authors also acknowledge partial support from the Australian Research Council (ARC) under project numbers CE230100032 and FL190100126, as well as the financial support of Vecor Technologies Pty Ltd. The authors further acknowledge the characterization facilities provided by the Mark Wainwright Analytical Center and the XRF Laboratory at UNSW Sydney, and the Australian Nuclear Science and Technology Organisation (ANSTO) Synchrotron.

Author contributions

X.Zheng designed and undertook the experimental work, characterization, and data analysis; wrote the initial draft of the manuscript; and worked on all subsequent drafts. S.S.Mofarah jointly supervised the project. R.F.Webster and S.L.Y.Chang assisted with the HRTEM/EELS work and the associated preliminary data analyses. J.Zhang undertook ZAB works. C. Cazorla undertook all of the DFT work, wrote the associated data analysis, and contributed to the final draft. Y.Nie assisted with the ORR work. L.Dai advised on the technical structure and contributed to the final draft. S.Wang, T.Zhao, and C.Zhao assisted with the OER work. J.Wang and D.Chu assisted with the XAS work. Y.Yao assisted with CAFM work. Y.Jiang, L. Sheppard and T.D. Villenoisy assisted with sample fabrication. P.Koshy supervised the project and worked on all subsequent drafts. C.C. Sorrell jointly supervised the project, provided the basis for the formal data analysis, and worked on all subsequent drafts.

Competing interests

The authors declare no competing interests.

Additional information

Supplementary information The online version contains supplementary material available at https://doi.org/10.1038/s41467-026-69849-4.

Correspondence and requests for materials should be addressed to Xiaoran Zheng, Sajjad S. Mofarah or Pramod Koshy.

Peer review information *Nature Communications* thanks Minjoon Park and the other anonymous reviewer(s) for their contribution to the peer review of this work. A peer review file is available.